

THE $Z = 5$ QUASAR LUMINOSITY FUNCTION FROM SDSS STRIPE 82

IAN D. MCGREER¹, LINHUA JIANG^{2,†}, XIAOHUI FAN¹, GORDON T. RICHARDS³, MICHAEL A. STRAUSS⁴, NICHOLAS P. ROSS⁵,
 MARTIN WHITE^{5,6}, YUE SHEN⁷, DONALD P. SCHNEIDER^{8,9}, ADAM D. MYERS¹⁰, W. NIEL BRANDT⁸, COLIN DEGRAFF¹¹,
 EILAT GLIKMAN¹², JIAN GE¹³, ALINA STREBLYANSKA^{14,15}

Draft version March 3, 2019

ABSTRACT

We present a measurement of the Type I quasar luminosity function at $z = 5$ using a large sample of spectroscopically confirmed quasars selected from optical imaging data. We measure the bright end ($M_{1450} < -26$) with Sloan Digital Sky Survey (SDSS) data covering $\sim 6000 \text{ deg}^2$, then extend to lower luminosities ($M_{1450} < -24$) with newly discovered, faint $z \sim 5$ quasars selected from 235 deg^2 of deep, coadded imaging in the SDSS Stripe 82 region (the celestial equator in the Southern Galactic Cap). The faint sample includes 14 quasars with spectra obtained as ancillary science targets in the SDSS-III Baryon Oscillation Spectroscopic Survey (BOSS), and 59 quasars observed at the MMT and Magellan telescopes. We construct a well-defined sample of $4.7 < z < 5.1$ quasars that is highly complete, with 73 spectroscopic identifications out of 92 candidates. Our color selection method is also highly efficient: of the 73 spectra obtained, 71 are high redshift quasars. These observations reach below the break in the luminosity function ($M_{1450}^* \approx -26.8$), although the faint-end slope is poorly constrained. The bright end slope is steep ($\beta \lesssim -3.5$), with a constraint of $\beta < -2.5$ at 95% confidence. The break luminosity appears to evolve strongly at high redshift, providing an explanation for the flattening of the bright end slope reported previously. We find a factor of ~ 2 greater decrease in the number density of luminous quasars ($M_{1450} < -26$) from $z = 5$ to $z = 6$ than from $z = 4$ to $z = 5$, suggesting a more rapid decline in quasar activity at high redshift than found in previous surveys. Our model for the quasar luminosity function predicts that quasars generate $\sim 20\%$ of the ionizing photons required to keep the universe ionized at $z = 5$.

Subject headings: quasars: general

imcgreer@as.arizona.edu

Observations reported here were obtained at the MMT Observatory, a joint facility of the Smithsonian Institution and the University of Arizona. This paper also includes data gathered with the 6.5-m Magellan Telescopes located at Las Campanas Observatory, Chile.

¹ Steward Observatory, The University of Arizona, 933 North Cherry Avenue, Tucson, AZ 85721-0065, USA

² School of Earth and Space Exploration, Arizona State University, Tempe, AZ 85287, USA

³ Department of Physics, Drexel University, 3141 Chestnut Street, Philadelphia, PA 19104, USA

⁴ Department of Astrophysical Sciences, Princeton University, Princeton, NJ 08544, USA

⁵ Lawrence Berkeley National Laboratory, 1 Cyclotron Road, Berkeley, CA 94720, USA

⁶ Department of Physics, 366 LeConte Hall, University of California, Berkeley, CA 94720, USA

⁷ Harvard-Smithsonian Center for Astrophysics, 60 Garden Street, Cambridge, MA 02138, USA

⁸ Department of Astronomy and Astrophysics, The Pennsylvania State University, 525 Davey Laboratory, University Park, PA 16802, USA

⁹ Institute for Gravitation and the Cosmos, The Pennsylvania State University, University Park, PA 16802, USA

¹⁰ Department of Physics and Astronomy, University of Wyoming, Laramie, WY 82071, USA

¹¹ McWilliams Center for Cosmology, Carnegie Mellon University, 5000 Forbes Avenue, Pittsburgh, PA 15213, U.S.A.

¹² Department of Physics and Yale Center for Astronomy and Astrophysics, Yale University, P.O. Box 208121, New Haven, CT 06520-8121

¹³ Dept. of Astronomy, University of Florida, 211 Bryant Space Science Center, Gainesville, FL, 32611, USA

¹⁴ Instituto de Astrofísica de Canarias (IAC), E-38200 La Laguna, Tenerife, Spain

¹⁵ Dept. Astrofísica, Universidad de La Laguna (ULL), E-38206 La Laguna, Tenerife, Spain

[†] Hubble Fellow

1. INTRODUCTION

The number density of quasars evolves strongly with redshift, a conclusion reached shortly after the initial identification of cosmological redshifts for quasars. Quasars increase in number with increasing redshift (Schmidt 1968) until $z \sim 2.5$, when quasar activity peaks, as surveys for higher redshift quasars show a steep decline in number (Osmer 1982; Warren et al. 1994; Schmidt et al. 1995; Fan et al. 2001b; Richards et al. 2006). Quasars are associated with accretion onto supermassive black holes (Salpeter 1964); how the first such black holes grew from initial seeds and were triggered by gas accretion to become luminous quasars remain key questions about the evolution of the early universe (see, e.g., the recent review by Volonteri 2010). Indeed, quasars are now observed to $z \sim 7$ (Mortlock et al. 2012), indicating that the mechanisms that drive them were in place within 0.8 Gyr after the Big Bang.

The quasar luminosity function (QLF) is one of the most fundamental observational probes of the growth of supermassive black holes over cosmic time. The QLF is generally found to have the form of a broken power law (Boyle et al. 1988; Pei 1995; Boyle et al. 2000), with a steep slope towards high luminosities and a flatter slope extending to low luminosities. Observed evolution in the shape of the QLF with redshift — e.g., a change in the power law slopes or the location of the break luminosity — may provide insight into the physics of black hole growth. Many studies have found evidence for evolution of the QLF in large quasar samples (Schmidt et al. 1995; Fan et al. 2001b; Richards et al. 2006; Hopkins et al. 2007b; Croom et al. 2009). One key consequence of this evolution is the observed “downsizing” of quasar activity: where by the spatial density of more luminous objects peaks at higher redshifts (Cowie et al. 2003; Ueda et al. 2003; Hasinger et al. 2005; Croom et al. 2009).

Theoretical models for quasars have explored a variety of physical processes that may drive the triggering of quasar activity. These models make testable predictions about the evolution of the QLF based on the evolution of the triggering mechanisms. For example, models where quasar activity is instigated by mergers of gas-rich galaxies (e.g., Hernquist 1989; Carlberg 1990; Cattaneo et al. 1999; Kauffmann & Haehnelt 2000; Hopkins et al. 2006; Shen 2009) tie the QLF to the evolution of the merger rate of dark matter halos in cosmological simulations. Alternatively, some hydrodynamical simulations point to rapid inflows of cold gas along filamentary structures in the cosmic web as the primary fueling mechanism at high redshift (e.g., Di Matteo et al. 2012). It is also possible to predict the QLF while being agnostic to the specific triggering mechanisms; Conroy & White (2012) describe a model for populating galaxies with accreting black holes that directly relates the evolution of quasars to that of their host galaxies.

Furthermore, feedback from black hole accretion is expected to play an important role in regulating the growth of black holes and the duration of quasar activity (e.g., Di Matteo et al. 2005; Hopkins et al. 2006). As the QLF is a convolution of the black hole mass function and the Eddington ratio¹⁷ distribution, these processes will alter the shape of the QLF (Hopkins et al. 2005). While the

low-redshift QLF is reasonably well measured by surveys at optical, X-ray, and mid-infrared wavelengths (see, e.g., the compilation of Hopkins et al. 2007b), observations at high redshift are less constraining on these models, even though it is at high redshift where, for example, different feedback models make significantly different predictions for the quasar population (Hopkins et al. 2007a). Feedback-regulated models for quasar activity tend to predict strong evolution of the bright-end slope with redshift (e.g., Kauffmann & Haehnelt 2000; Wyithe & Loeb 2003), and also provide a physical explanation for the observed downsizing trend Scannapieco et al. (2005).

Measurements of the high redshift QLF also allow estimates of the contribution of quasars to the ionization state of the intergalactic medium (IGM) during and after reionization. Quasars are unlikely to produce enough ionizing photons to be the primary driver of reionization (Fan et al. 2001a) although current constraints on the quasar ionizing photon budget are limited to extrapolations from the bright end of the QLF and a handful of faint $z \sim 6$ quasars (Jiang et al. 2009; Willott et al. 2010), as well as upper limits on moderate luminosity AGN from X-ray surveys (Barger et al. 2003; Fontanot et al. 2007). Quasars do have a much harder spectrum than stellar sources, but constraints from the soft X-ray background limit the contribution of high energy photons to large-scale reionization (Dijkstra et al. 2004; McQuinn 2012). Nonetheless, there are few observational constraints on the faint quasar population during the epoch of reionization. And while quasars may not be directly responsible for hydrogen reionization, they are expected to provide the high-energy photons responsible for He II reionization at lower redshifts (e.g., Haiman & Loeb 1998; Madau et al. 1999; Miralda-Escudé et al. 2000). Models of IGM evolution thus benefit from improved observational constraints on quasar activity at high redshift (e.g., Bolton et al. 2009).

Currently, only optical and near-IR imaging surveys provide the requisite area and depth to construct large samples of quasars at high redshifts (see, e.g., the compilation given in Ross et al. 2012). Throughout most of the 1990s, the redshift record was held by a 19th magnitude quasar at $z = 4.9$ (Schneider et al. 1991). The first quasar with $z \geq 5$ was discovered by Fan et al. (1999) in commissioning data from the Sloan Digital Sky Survey (SDSS; York et al. 2000). The same data were used to build a sample of 39 quasars with $3.6 < z < 5.0$ to a limit of $i = 20$ (Fan et al. 2001b) and to study the evolution of quasars at high redshift, confirming the steep decline in number density at $z > 3$ (roughly a factor of three per unit redshift). The early high-redshift quasar surveys also found evidence for flattening of the bright-end slope relative to lower redshifts (Schmidt et al. 1995; Fan et al. 2001b), a result seemingly confirmed by a large, homogeneous quasar sample from the SDSS extending to $z = 5$ (Richards et al. 2006). This type of evolutionary trend in the bright-end slope would contribute to a downsizing effect, by slowing the decline in number density with redshift for quasars above the break luminosity.

The SDSS-III Baryon Oscillation Spectroscopic Survey (BOSS; Eisenstein et al. 2011; Dawson et al. 2012) aims to collect spectra of over 150,000 quasars with red-

¹⁷ The ratio of the mass accretion rate onto the black hole to

the maximal rate allowed by the Eddington limit.

shifts between 2.2 and 3.5. Ross et al. (2012) present the QLF measured from 22,000 color-selected quasars from BOSS DR9, as well as two samples of variability-selected quasars at $z < 3.5$ from Palanque-Delabrouille et al. (2011) and Palanque-Delabrouille et al. (2012). The BOSS spectroscopic target selection extends ~ 1.5 mag fainter than the SDSS, reaching below the break in the luminosity function to $z \sim 3.5$. Combined with the 2SLAQ (Croom et al. 2009), these large quasar surveys form a fairly complete picture of the optically unobscured (Type I) quasar population at $z \lesssim 3$.

At higher redshifts, over 50 quasars are now known at $z \gtrsim 6$. While constraints at these redshifts are weaker (and await future wide-area surveys for greater numbers), the best determinations to date indicate that the bright-end slope is steep (Jiang et al. 2008; Willott et al. 2010), roughly agreeing with the $z < 3.5$ measurements from BOSS and the $z \sim 2.5$ determination from Croom et al. (2009). One of the aims of this work is to examine the QLF at intermediate redshifts and test previous claims for a flattening of the bright-end slope at $z > 3$.

We present a measurement of the QLF at $z = 5$, combining bright quasars from the SDSS with faint quasars reaching nearly 2 mag deeper. These quasars are drawn from optical imaging data (probing the rest-frame ultraviolet) and thus have low intrinsic extinction, and are confirmed by spectroscopy to be broad emission line, Type I quasars. The faint sample is derived from coadded optical imaging in the SDSS Stripe 82 region. This imaging covers 235 deg^2 to a depth more than 2 mag fainter than the SDSS main survey. The combination of medium depth and medium sky area – relative to SDSS and to small-area deep fields – is ideal for searching for rare, faint high-redshift quasars. With Stripe 82 we are able to reach sufficient depth to probe the faint end of the luminosity function, while attaining enough dynamic range to constrain its overall shape. This uniform sample of $z \sim 5$ quasars – selected with simple criteria over a homogeneous imaging area – is larger than all $z \gtrsim 6$ surveys combined, and provides a key link in our understanding of quasar evolution at high redshift.

We first describe the coadded optical images on Stripe 82 that provide the primary catalogs from which we select candidates, as well as infrared imaging from UKIDSS and our own observations used to reduce stellar contamination (§ 2). Section 3 outlines our selection criteria, derived from models of quasar colors, and based on simple color cuts. We combine spectroscopy from the SDSS and BOSS surveys with our own observations using the MMT and Magellan telescopes to build a sample of over 70 $z \sim 5$ quasars to a limit of $i_{\text{AB}} = 22$; the observations and data processing are presented in section 4 and the catalog of quasars is provided in section 5. In section 6 we use our quasar color model to quantify the completeness of the survey; with this in hand we calculate the binned luminosity function and derive a parametric form for the luminosity function using the maximum likelihood technique. We explore the evolution of the QLF at high redshift and determine the contribution of quasars to the ionizing background at $z \sim 5$ based on our QLF model. We present conclusions in section 7.

We incorporate photometric data from several sources

in this work; for consistency, all magnitudes are converted to the AB system (Oke & Gunn 1983) unless otherwise noted. SDSS reports *ugriz* photometry on the asinh scale (Lupton et al. 1999), which is nearly identical to AB at bright magnitudes. Although we use SDSS photometry only for bright quasars, we will note any instances where the asinh system is used. We refer to the SDSS DR7 imaging as “SDSS main”, in contrast to the deep imaging we use to build our primary faint quasar sample, referred to as “Stripe 82” or “the coadd imaging” (§2.1). UKIDSS magnitudes are Vega-based, but we convert all UKIDSS magnitudes to AB using the values given in Hewett et al. (2006). All magnitudes are corrected for Galactic extinction (Schlegel et al. 1998) unless otherwise noted. We use a Λ CDM cosmology with parameters $\Omega_{\Lambda} = 0.728$, $\Omega_m = 0.272$, $\Omega_b = 0.0456$, and $H_0 = 70 \text{ km s}^{-1} \text{ Mpc}^{-1}$ (Komatsu et al. 2009).

2. IMAGING DATA

2.1. Stripe 82 coadded imaging

Over the ten year duration of the survey, the SDSS I/II repeatedly imaged a $2^\circ 5' \times 100''$ stripe centered at zero declination in the Southern Galactic Cap (Abazajian et al. 2009). This repeat imaging increased in frequency during the latter part of operations as part of the SDSS Supernova Survey (Frieman et al. 2007). By the end of operations, over 100 repeat imaging scans were obtained along Stripe 82 (its designation according to the survey geometry, Stoughton et al. 2002). As with the main survey, the imaging was obtained with a drift-scan camera (Gunn et al. 1998) mounted on the 2.5m Sloan telescope (Gunn et al. 2006), with nearly simultaneous 54.1 s exposures in five broad optical bands (*ugriz*; Fukugita et al. 1996). The quality restrictions applied to the main survey imaging (photometric and good-seeing conditions; Ivezić et al. 2004; Hogg et al. 2001) were relaxed for the Supernova Survey in order to increase the temporal coverage, resulting in a greater range of data quality.

Jiang et al. (2009) describe deep *riz* images of Stripe 82 constructed from the coaddition of 50-60 individual imaging scans at each position on the sky. Images with seeing poorer than $2''$ or an *r*-band sky background brighter than $19.5 \text{ mag arcsec}^{-2}$ were rejected. The remaining images were weighted by their transparency, seeing, and sky background noise, and coadded using the SWARP software (Bertin et al. 2002). The final coadded images reach a depth roughly 2 mag fainter than single-epoch SDSS images, and were used to discover $z \sim 6$ quasars as faint as $z_{\text{AB}} = 22.2$ (Jiang et al. 2009). These data are not the only coadded images available for Stripe 82: Annis et al. (2011) produced coadded images made using a similar process but with stricter image quality criteria resulting fewer imaging scans used at each sky position, while Huff et al. (2011) created image stacks optimized for weak lensing shear studies.

Our starting point is the *riz* coadded images from Jiang et al. (2009), which we now extend to include the *u* and *g* bands (Jiang et al., in preparation). The deep imaging in the bluer SDSS bands is being used to discover ultra-luminous Lyman break galaxies at $z > 2.5$ (Bian et al., in preparation). In this work, we extend the Jiang et al. (2009) search for faint, $z \sim 6$ quasars to

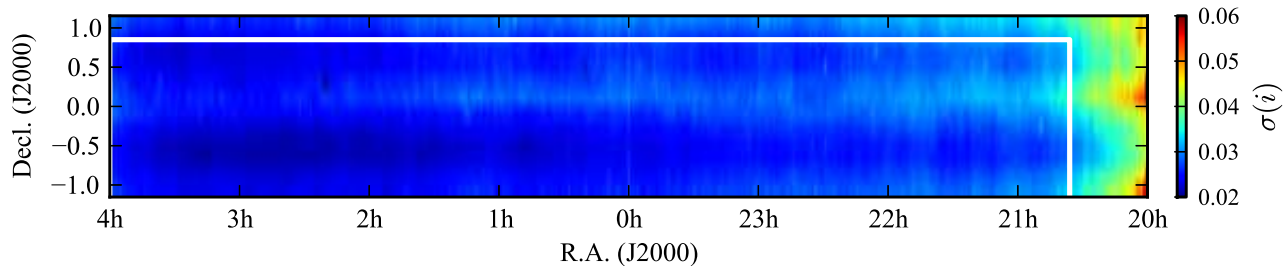


FIG. 1.— Median photometric uncertainty for stars with $i = 22$ along Stripe 82. The depth is very uniform, and with a typical uncertainty of $\sigma(i) \approx 0.03$ at the flux limit for our quasar survey the completeness is high. We search for quasar candidates within the region bounded by the white lines. The cutoff at R.A. = $20^{\text{h}} 32^{\text{m}}$ is due to the high stellar density along the western edge of Stripe 82, as well as the lack of UKIDSS coverage there. Note that the photometric uncertainties increase outside the boundary, likely due to crowding in the high stellar density regions. The cutoff at $\delta = 0.85^\circ$ is due to problems in the g -band coadded images in the northernmost two camera columns of the Stripe.

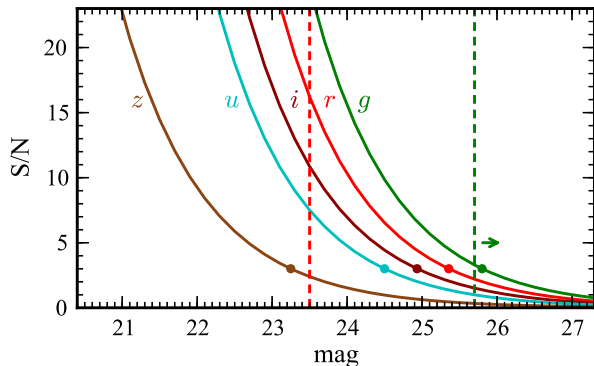


FIG. 2.— Stripe 82 coadded imaging depth in the five SDSS bands. Lines represent the median S/N measured in $1.8''$ apertures for isolated stellar objects (no extinction correction has been applied). Filled circles are drawn at the 3σ limits. The vertical dashed lines show the approximate r (red) and g (green) magnitudes for a typical $z \sim 5$ quasar at our survey limit of $i = 22$, based on colors of $r - i = 1.5$ and $g - r \geq 2.2$. By comparison, the 95% completeness limits for single-epoch SDSS imaging are $g \approx 22.2$, $r \approx 22.2$, and $i \approx 21.3$ (Stoughton et al. 2002). The depth of the coadded imaging in the g band allows for reliable selection of very red objects.

lower redshifts ($z \sim 5$), as the deep g -band photometry combined with the redder bands allows reliable color selection of quasars in this redshift range. The depth of our coadds is similar to that of the Annis et al. (2011) coadds (see their Fig. 7); however, as described in §4.2 we encountered much greater contamination when using the catalogs from the Annis et al. (2011) coadds for quasar selection.

We use SExtractor (Bertin & Arnouts 1996) to produce object catalogs from the deep $ugriz$ images. Object detection was performed in the i -band, and fluxes and other measurement parameters in the other bands were derived from apertures centered on the i -band object position using the dual-image mode of SExtractor. All fluxes and magnitudes from the coadded Stripe 82 imaging quoted in this work are taken from aperture photometry using a $1.8''$ diameter. The typical seeing in the coadded images¹⁸ is $1.4''$, $1.3''$, $1.1''$, $1.0''$, and $1.1''$ in u , g , r , i , and z , respectively.

The geometry of the Stripe 82 coadded imaging fol-

lows that of the parent SDSS imaging¹⁹. We photometrically calibrated individual fields in the coadded catalogs by deriving zero points from the übercalibrated (Padmanabhan et al. 2008) SDSS DR8 (Aihara et al. 2011) photometry (derived from the best individual imaging scan at each location in Stripe 82), using stars with $15.5 < r < 20.5$. We thus tie the aperture photometry from SExtractor on a field-by-field basis to PSF photometry from SDSS. This process results in zero points that account for seeing and photometric variations between the fields, but not within the fields. However, the large number of images contributing to the coadds tends to average over effects such as varying sky backgrounds and PSF shapes. In general, we find the photometry is highly consistent between fields and agrees quite well with SDSS photometry for the brighter objects. Figure 1 shows that the depth across the Stripe is highly uniform, and Figure 2 shows the depths reached in the $ugriz$ bands in the coadded imaging.

Quasars at $z \sim 5$ have similar fluxes in the i and z bands. We adopt the i -band as our detection band as it provides greater a greater signal-to-noise ratio. However, at $z \sim 5$ the Ly α emission line and the Ly α forest are within the i -band. The fluxes in the band that defines our detection threshold are thus subject to the substantial variances in Ly α equivalent widths, the incidence of strong Ly α absorption systems, and variations in the mean IGM opacity. The z -band is less affected by these issues (although it does contain C IV in emission); however, it is significantly noisier than the i -band because of lower CCD sensitivity and a higher sky background. We will discuss these issues further in §5.

We further note that our survey is restricted to less than the full area on Stripe 82 for two reasons. At the time that we performed target selection, the coadds corresponding to the two uppermost camera columns had problems with the sky background in the g -band, rendering them inadequate for our purposes. We thus imposed a cutoff of $\delta < 0.85^\circ$ when selecting candidates. In addition, the western edge of Stripe 82 (near 20^{h}) approaches the Galactic plane. Attempting color se-

¹⁸ The weighting scheme used when coadding the images favors better seeing data; it is $w = T \times (\text{FWHM}^2 \sigma^2)^{-1}$, where T is the transparency, FWHM is the full width at half-maximum of the point-spread function (PSF), and σ^2 is the variance of the sky background (Jiang et al. 2009).

¹⁹ The SDSS camera consists of six columns of CCDs that are continuously exposed in a drift-scan mode (Gunn et al. 1998). The gaps between the CCD columns are filled by combining two Strips offset in declination (each consisting of a single scan) to form a Stripe. Thus the declination axis of Stripe 82 is split into 12 columns during the imaging scans. Each scan is $13'$ wide in declination, broken into $10'$ segments along right ascension; these image segments are referred to as fields.

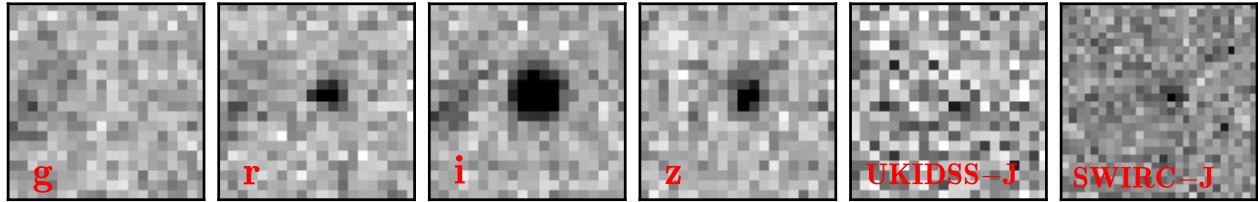


FIG. 3.— Example images of a typical faint quasar at $z = 4.9$ selected by this survey. The panels contain the *griz* coadded imaging, followed by the UKIDSS *J* image, and a *J* image from MMT/SWIRC. This object (J234601.5-003855) is not detected in the *g*-band, and has $r = 23.64 \pm 0.09$, $i = 21.72 \pm 0.02$, and $z = 21.74 \pm 0.08$. It is undetected in UKIDSS; the SWIRC imaging yields $J = 21.39 \pm 0.13$. In the best single-epoch imaging from SDSS DR8, this object is a $\sim 9\sigma$ detection in the *i*-band and $\lesssim 3\sigma$ in *r* and *z*.

lection of quasars in this region would result in overwhelming stellar contamination (see, e.g., Figure 1 of Vanden Berk et al. 2005). We thus restrict our survey to objects with R.A. $> 20^{\text{h}} 32^{\text{m}}$ (this region also lies outside the UKIDSS imaging area described in the next section). The final area of the deep imaging we used for $z \sim 5$ quasar selection is 235 deg^2 , extending from $20^{\text{h}} 32^{\text{m}}$ to 4^{h} , and from -1.25° to $+0.85^\circ$ (Fig. 1).

2.2. UKIDSS

The UKIRT Infrared Deep Sky Survey (UKIDSS; Lawrence et al. 2007) consists of multiple infrared imaging surveys with the UKIRT Wide Field Camera (WFCAM; Casali et al. 2007), including a wide-area component (the Large Area Survey or LAS) that covers $\sim 4000 \text{ deg}^2$ to a depth of $J_{\text{AB}} \approx 20.6$ (5σ). The LAS includes Stripe 82, providing shallow infrared imaging of our candidates and additional leverage in discriminating high redshift quasars from stellar contaminants. We first apply a loose color cut to identify potential quasar candidates from the coadded optical imaging,

$$(r - i) > 1.0 \quad \&\& \quad (i - z) < 0.625[(r - i) - 1.0] + 0.2,$$

then queried the DR8plus release in the WFCAM Science Archive (WSA; Hambly et al. 2008) for infrared counterparts.

Quasars at $z \sim 5$ have $(i - J)_{\text{AB}} \sim 0$ (see section 3), thus at the faint limit of our survey most of our target objects do not have a counterpart in the UKIDSS catalogs. However, stars with similar optical colors to $z \sim 5$ quasars (namely, M and L dwarf stars) are redder in the near-IR ($0.5 < (i - J)_{\text{AB}} < 1.5$, see Fig. 5) and thus are relatively brighter at infrared wavelengths. We downloaded *J*-band image cutouts from the WSA for all of the candidates pre-selected from the optical imaging, then performed aperture photometry using the IRAF *aper* task at the *i*-band position from the SDSS coadded imaging, measured in $2''$ diameter apertures. We validated our photometry by checking against the UKIDSS catalog measurements for brighter objects (utilizing the UKIDSS calibration as described in Hodgkin et al. 2009). The aperture photometry reaches $J \approx 21.3$ at 3σ , sufficient to discriminate the typical stellar contaminants at our limit of $i = 22$. Thus the IR information is highly useful as stellar veto: of the $\sim 10,000$ pre-selected candidates from the optical imaging, only ~ 650 are rejected by the $i - J$ color cut we adopt (§3.2) using the UKIDSS catalog photometry, while ~ 4500 are rejected based on the aperture fluxes.

2.3. MMT SWIRC

At the time the initial candidate selection was performed, the publicly available UKIDSS data on Stripe 82 did not extend to R.A. $< 21^{\text{h}} 36^{\text{m}}$. We imaged some of the candidates lacking *J* coverage on 2011 Oct 14-15 with the MMT Smithsonian Widefield Infrared Camera (SWIRC; Brown et al. 2008). Each object was observed in the *J* band using a 9-point dither pattern with 30s exposures at each position, for a total integration time of 4.5 min. The typical seeing was $0.6\text{--}0.9''$. Images were dark-corrected, flat-fielded, sky-subtracted, shifted, and combined using standard IRAF routines. Object photometry was measured in $2''$ diameter apertures using IRAF routines, and calibrated using observations of UKIRT Faint Standards.

A total of 38 objects were observed with SWIRC. This includes 10 objects already spectroscopically confirmed as quasars but that lacked UKIDSS coverage or had low *S/N* in the *J*-band. These objects were observed as a check on our *J*-band color selection for quasars selected solely by optical colors. The remaining SWIRC targets were taken from a sample of objects selected as high-redshift quasar targets based on optical colors but that lacked UKIDSS coverage. These objects are mainly at $309^\circ < \alpha_{\text{J2000}} < 360^\circ$, the region of our survey with the highest stellar density. Nearly all of these sources were readily identified as stellar contaminants from bright detections in the SWIRC imaging, and would have greatly reduced the purity of our spectroscopic sample had they not been observed with SWIRC.

Figure 3 displays postage stamp images of a typical quasar within our survey. The *i*-band clearly has the highest *S/N*. The non-detection in UKIDSS and the faint detection in the deeper SWIRC imaging are expected for a $z \sim 5$ quasar; a contaminating star would have been easily identified from the infrared imaging.

3. QUASAR CANDIDATE SELECTION

Quasars are typically selected from imaging data using their colors, but these colors are a strong function of redshift, and overlap with the stellar locus at certain redshifts (Fan 1999; Richards et al. 2001, 2002). Optimal techniques have been developed for extracting the much rarer quasar population from the overwhelming contamination due to stars within the Galaxy. The probability that an object is a quasar or star can be determined by considering the local density of quasars and stars in the multidimensional space defined by the set of fluxes available from an imaging survey. These probabilities can be used to efficiently select quasar candidates (Bovy et al. 2011; Kirkpatrick et al. 2011). Similar techniques have also been applied at high redshift, where the problem is

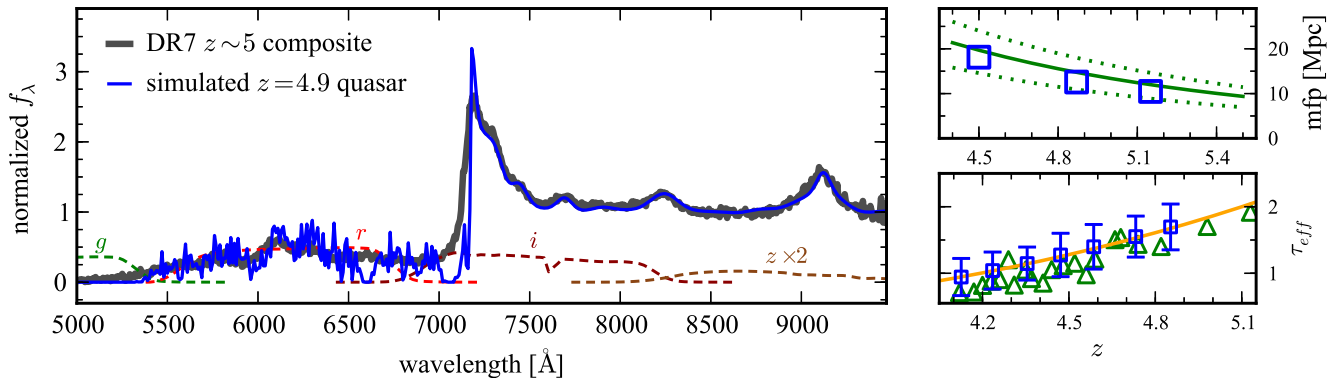


FIG. 4.— Left panel: example simulated quasar spectrum at $z = 4.9$ (blue) compared to a composite spectrum of DR7 quasars with $4.7 < z < 5.1$ (gray, shifted to $z = 4.9$). The simulated quasar spectrum was randomly drawn from the simulation grid described in §3.1, and selected to have $M_{1450} = -26.5$, roughly the median luminosity of $z \sim 5$ DR7 quasars. The simulated Ly α forest is calculated at a resolution of 0.1 \AA ; here the spectrum is rebinned to 10 \AA . This line of sight includes two strong DLAs ($\log N_{\text{HI}} \sim 21.1$) at $z = 4.428$ and $z = 4.808$. The SDSS filter curves are shown as a reference for which parts of the spectrum contribute to the broadband colors. Upper right panel: the mean free path in proper Mpc from the simulations, represented by blue squares. The solid green line represents the evolution in the mfp derived by Songaila & Cowie (2010), along with the $\pm 1\sigma$ range (dotted lines). Lower right panel: the effective optical depth (τ_{eff}) from the simulations, represented as blue squares with error ranges indicating the scatter among 1000 simulated lines-of-sight. Measurements from Songaila (2004) are shown as green triangles, and the evolution derived by Fan et al. (2006a) is shown by a solid orange line. We converged on a forest model with mfps $\sim 10\%$ lower than the mean values from Songaila & Cowie (2010); however, the τ_{eff} measurements are highly consistent with the observations.

worsened by the extreme rarity of quasars and the small number of bands in which the candidates are detected, typically at low S/N (Mortlock et al. 2012).

Fortunately, at $z \sim 5$ quasar colors are well separated from those of stars. At $z > 4.6$ the r -band is completely within the Ly α forest and the $r-i$ colors of quasars shift markedly redward of the stellar locus, while the $i-z$ colors sample the Ly α to C IV region of the rest-frame UV and are bluer than the stellar locus. The g -band samples the Lyman limit; $g-r$ colors are generally redder than those of stars due to the mean forest absorption; furthermore, most quasars will encounter a Lyman Limit System (LLS) near the red edge of the g -band, leading to saturated absorption and a g -band non-detection. Simple color selection at these redshifts was used in the SDSS I/II (Richards et al. 2002), leading to the first quasars discovered at $z > 5$ (Fan et al. 1999) and a total of over 300 $z > 4.6$ quasars by the DR7 release (Schneider et al. 2010).

In this section, we describe a model for quasar colors based on simulated quasar spectra. We use these model quasar colors to motivate our simple color cuts that achieve a high degree of both completeness and purity.

3.1. Simulated quasars

Fan (1999) outlines a procedure for generating simulated quasar spectra using a simple empirical model for their spectral properties at UV/optical wavelengths. The simulated spectra are integrated through survey bandpasses to generate simulated fluxes (colors) that can be used to define selection criteria, and to estimate their completeness. This requires that the spectral model reliably captures the diversity of quasar spectral features, and thus accurately reproduces observed quasar colors. The basic components of the quasar model are a broken power-law continuum, prominent UV/optical emission lines, pseudo-continuum from Fe complexes, and redshift-dependent Ly α forest absorption due to intervening neutral hydrogen. We have used an updated version of this model (described below) to reproduce the

colors of $\sim 60,000$ quasars from the SDSS-III/BOSS in the range $2.2 < z < 3.5$ (Ross et al. 2012). We apply the model at higher redshift under the assumption that the distribution of quasar SEDs does not evolve with redshift (Kuhn et al. 2001; Yip et al. 2004; Jiang et al. 2006). This approach can be compared to, e.g., cloning the spectra of lower redshift quasars to higher redshift (Chiu et al. 2005; Willott et al. 2005), which carries with it any selection function imprinted on the lower redshift sample; or using a small set of quasar templates (Mortlock et al. 2012), which may not capture objects with unusual features.

Each quasar is assigned a power law continuum with a break at 1100 \AA . The blue slope is drawn from a normal distribution with $\mu(\alpha) = -1.7$ and $\sigma(\alpha) = 0.3$ (Telfer et al. 2002); the distribution for the red slope is $\mu(\alpha) = -0.5$ and $\sigma(\alpha) = 0.3$. We add to this continuum emission lines with Gaussian profiles, where the Gaussian parameters (wavelength, equivalent width, and FWHM) are drawn from normal distributions. These distributions are derived from fitting composite spectra of BOSS quasars in luminosity bins. These distributions recover trends in the mean and scatter of the line parameters as a function of continuum luminosity, e.g., the Baldwin Effect (Baldwin 1977), and blueshifted lines (Gaskell 1982; Richards et al. 2011). Finally, we include Fe emission using the template of Vestergaard & Wilkes (2001), scaling the template in segments to match the Fe emission in the composite spectra. We do not include a contribution from quasars with unusually weak emission lines, which account for $\sim 6\%$ of quasars at $z > 4.2$ (Diamond-Stanic et al. 2009), or from Broad Absorption Line (BAL) quasars, which tend to have moderately redder colors (e.g., Weymann et al. 1991; Brotherton et al. 2001; Reichard et al. 2003).

The quasar model for the BOSS employs a prescription for the Ly α forest based on the work of Worseck & Prochaska (2011). This forest model is calibrated to observations at $z < 4.6$. We extend the model to higher redshifts by using the observed

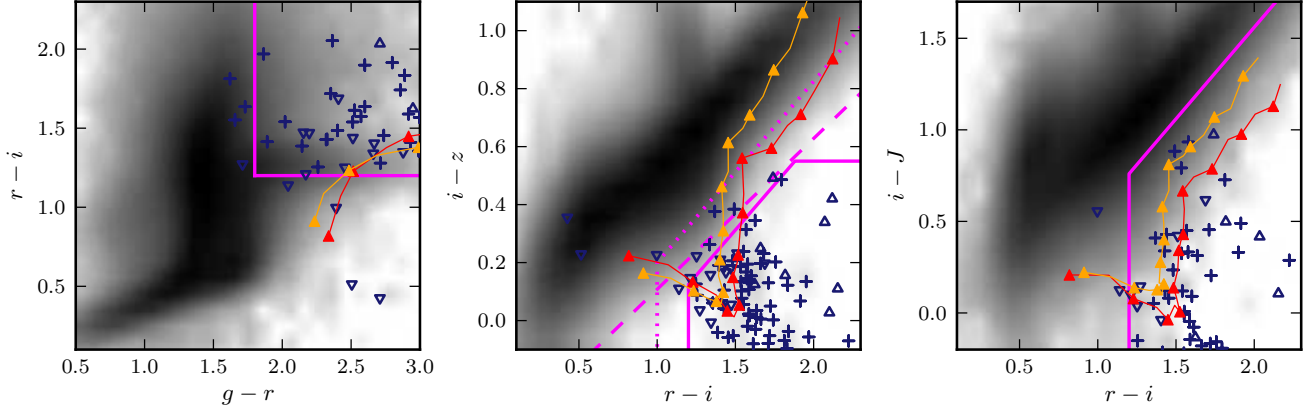


FIG. 5.— Selection criteria for $z \sim 5$ quasars. The background image shows the density of isolated point-like objects on Stripe 82 with $i < 22$ and $\sigma(u) < 2.5$ (i.e., u -band dropouts); a logarithmic scaling has been applied. These objects represent the red end of the stellar locus and are our primary source of contamination. Overlaid are the mean color tracks for quasars from $z = 4.5$ to $z = 5.5$, in steps of $\Delta z = 0.1$. The colors are derived from our simulations and include the luminosity dependence of emission line strengths; the two tracks are for $M_{1450} = -26.7$ (orange) and $M_{1450} = -24.5$ (red). The solid magenta lines are the color selection criteria used to identify $4.7 < z < 5.1$ quasars on Stripe 82. In the middle panel (riz colors), the dashed line shows the SDSS criteria used to target $z > 4.6$ quasars and adopted here for the analysis of DR7 quasars, and the dotted line shows our pre-selection criteria used to reduce the list of point-like objects for which we obtain aperture photometry in the UKIDSS J band. Finally, the purple points show spectroscopically confirmed $z > 4.5$ quasars on Stripe 82, with downward pointing triangles denoting $z < 4.7$ quasars, upward pointing triangles $z > 5.1$ quasars, and crosses quasars within our primary redshift range of $4.7 < z < 5.1$.

number densities of high column density systems from Songaila & Cowie (2010). For the lower column density systems ($\log N_{\text{HI}} < 17.2$), we begin with the parameters of Worseck & Prochaska (2011), and follow their method of deriving the number densities by simulating a large number of sight lines and matching the mean free paths (mfps) of the simulated sightlines to the observations of Songaila & Cowie (2010). We also force continuity between the column density distribution function ($dn/dN_{\text{HI}}dz$) at low and high column densities, and check the derived effective optical depth (τ_{eff}) against the measurements of Songaila (2004) and Fan et al. (2006a). There remains significant uncertainty in forest parameters at high redshift, but our simple color selection method is relatively insensitive to the model for the Ly α forest. To account for the degree of uncertainty in the forest absorption, we also include a “low” and “high” forest model, scaling the number densities of forest absorbers up and down by 10%, matching the scatter in measurements by Songaila & Cowie (2010). After comparison with observed quasar colors, we find that the model with a mean forest density 10% greater than the best-fit value from the mfp measurements provides the best match. Figure 4 shows an example simulated quasar spectrum from our models, and compares the Ly α forest observables (mfp and τ_{eff}) obtained from our simulated forest spectra to observations of high redshift quasars.

3.2. Color Selection

Based on the results from the simulated spectra, we concluded that the most efficient use of telescope time was to focus on a fairly narrow redshift range, $4.7 < z < 5.1$, where the colors of stars and quasars are best separated and the selection efficiency is high. Figure 5 shows the gri , riz , and riJ colors of red stars and high redshift quasars in our sample, as well as the selection criteria we adopted:

- $i < 22.0$
- $S/N(u) < 2.5$

- $g - r > 1.8$ OR $S/N(g) < 3.0$
- $r - i > 1.2$
- $i - z < 0.625((r - i) - 1.0)$
- $i - z < 0.55$
- $i - J < ((r - i) - 1.0) + 0.56$

where all magnitudes are in the AB system, measured within fixed apertures (as described in §2), and have been corrected for Galactic extinction using the maps of Schlegel et al. (1998). S/N measurements are obtained from the aperture fluxes and uncertainties given by SExtractor.

We apply no morphological criteria in our candidate selection after finding that the number of potentially resolved objects (SExtractor CLASS_STAR < 0.8) is small ($< 10\%$ of the total selected), indicating that contamination from compact galaxies is negligible.

These criteria are similar but not identical to the cuts that define the $z > 4.5$ inclusion region in the SDSS quasar selection algorithm, as given in Richards et al. (2002). We extend the selection nearly 2 mag fainter than the SDSS main survey by utilizing the coadded imaging on Stripe 82. We define dropout criteria in the u and g bands through S/N criteria within fixed apertures rather than a magnitude cut. Although the Stripe 82 coadded imaging is highly uniform (e.g., Fig. 1), using a S/N threshold more fully utilizes the u -band depth at a given location, as $z \sim 5$ quasars are not expected to have any detectable flux in this band. We bracket the redshift range of the search to $z \gtrsim 4.7$ by requiring a red $r - i$ color and to $z \lesssim 5.1$ by requiring a blue $i - z$ color. Finally, we take advantage of the available infrared data from UKIDSS, effectively imposing a veto on objects that are too red in $i - J$. This cut is made using the aperture flux ratios in the i and J bands, so that objects undetected in the UKIDSS J band — as expected for $z \sim 5$ quasars — pass the final cut without imposing a S/N threshold.

The i -band detection catalog contains 1.5M objects. We apply loose pre-selection cuts in the riz colors (see middle panel of Fig. 5 and §2.2) to reduce this list to $\sim 10,000$ potential candidates for which UKIDSS images are downloaded and analyzed. After applying the final criteria listed above, we have 92 candidates to a limit of $i_{AB} = 22$.

4. SPECTROSCOPIC OBSERVATIONS AND DATA REDUCTION

We obtain spectroscopic identifications of our candidates from multiple sources by utilizing the dense SDSS/BOSS spectroscopic coverage of Stripe 82 combined with our own observations. First, we identify a few of the brightest candidates on Stripe 82 using spectroscopic data from the SDSS I/II (Abazajian et al. 2009). More recently, the BOSS collected a large number of spectra on Stripe 82, including several ancillary science programs (Dawson et al. 2012) targeting high redshift quasars. Finally, we have obtained spectra for additional candidates (extending much fainter than the SDSS and BOSS spectroscopic observations) using the MMT and Magellan telescopes. In total, we have 73 spectroscopic identifications for our 92 candidates (79%). Table 1 summarizes the status of spectroscopic observations of $z \sim 5$ quasar candidates on Stripe 82, including a number of confirmed quasars not within the uniform sample.

4.1. SDSS DR7

The SDSS I/II spectroscopic survey concluded with the DR7 release (Abazajian et al. 2009). Spectra were reduced with the standard SDSS pipeline (Stoughton et al. 2002). Quasar target selection is described in Richards et al. (2002); high-redshift quasars are targeted through two methods, both to a limit of $i = 20.2$. First, outliers from the stellar locus in $griz$ space are identified as high-redshift quasar candidates, and second, various color cuts aim to extend the quasar yield within specific redshift ranges beyond the locus outlier selection. Schneider et al. (2010) present a catalog of over 100,000 spectroscopically confirmed quasars drawn from $\approx 9380 \text{ deg}^2$ of the DR7 spectroscopic footprint (hereafter DR7QSO). This catalog includes 191 quasars at $4.7 < z < 5.1$ to a limit of $i \lesssim 20.2$, of which 184 are selected by our color criteria based on their SDSS flux measurements.

We utilize the DR7 data in several ways. First, we matched our candidate list to the DR7QSO catalog, as well as to the full DR7 spectroscopic database. We identified eight of our candidates as confirmed $4.7 < z < 5.1$ quasars in DR7QSO. There were three additional quasars in this redshift range that did not meet our color criteria. None of our candidates matched to non-quasars among the 1.6 million objects with spectra in DR7.

We further employ the DR7 quasars to determine the bright end of the luminosity function, by constructing a uniform sample of DR7QSO quasars in our redshift range drawn from the SDSS DR7 imaging footprint. We will describe this sample in §6.1.1.

4.2. BOSS

The BOSS quasar survey is primarily designed to find quasars at $2.2 < z < 3.5$ for the purpose of $\text{Ly}\alpha$ forest

studies (McDonald & Eisenstein 2007; Ross et al. 2012). The Extreme Deconvolution algorithm (XDQSO) used as the primary quasar targeting method in BOSS is tuned to this redshift range and is highly efficient (Bovy et al. 2011). However, a large section of Stripe 82 was observed by BOSS in Fall 2010 as BOSS Chunk 11 (Ross et al. 2012); during these observations quasars were targeted through a combination of color selection (using XDQSO) and variability selection (Palanque-Delabrouille et al. 2011). The highest redshift quasar identified by the main BOSS targeting in Stripe 82, including variability, is at $z = 4.46$.

In addition, we are conducting ancillary science programs in BOSS that take advantage of unused fibers once the primary survey targets (galaxies and mid- z quasars) have been allocated fibers (Dawson et al. 2012). These programs extend the $griz$ and riz color cuts described in Richards et al. (2002) to fainter quasars by utilizing areas with multiple epochs of imaging in SDSS I/II due to overlapping or repeated scans. On Stripe 82 these ancillary programs utilized photometry from the ~ 20 -epoch coadded images available in the DR7 CAS and described in Annis et al. (2011); these observations are included in BOSS DR9 (Ahn et al. 2012). We will analyze the quasars identified in overlap regions outside of Stripe 82 in future work.

The selection criteria for $z > 4.6$ quasars are similar to the riz inclusion region in Richards et al. (2002), but extended to a faint limit of $i = 21.5$ and using the catalogs from the Annis et al. (2011) coadded imaging for target selection. On Stripe 82, this program was allocated 283 targets, of which 221 received spectra, but only 22 were high- z quasars. Of those, 10 were previously known from SDSS DR7; thus the program yielded only 12 new quasars. All 12 meet our selection criteria and are included in this study. The ancillary program targets that are not quasars fall mainly into two categories: 1) objects with fluxes contaminated by nearby bright stars, and 2) spurious or moving objects (e.g., asteroids). We matched the failed targets to the coadded image catalogs and found that either they did not have matches in our coadded imaging, or the matches did not meet our selection criteria.

BOSS spectra are collected with a fiber-fed, multi-object spectrograph (Smee et al. 2012) and reduced with a pipeline described in Bolton et al. (2012). We visually examined all of the spectra for ancillary program targets on Stripe 82, as well as any classified by the pipeline as having $z > 3.6$. We also cross-checked our examinations against the DR9 Quasar Catalog as described in Pâris et al. (2012). As with SDSS, we cross-checked our candidate list against all spectra in BOSS, not just confirmed quasars, again finding no matches to non-quasars. Figure 19 displays the BOSS spectra of $z > 4.7$ quasars on Stripe 82.

4.3. Magellan observations

The remaining candidates on Stripe 82 (~ 70) were mostly fainter than $i = 21$ and required spectroscopic observations on larger telescopes. We first observed four candidates at the Magellan Clay 6.5m on 2011 Jun 11-13 using the Magellan Echellette spectrograph (MAGE; Marshall et al. 2008). MAGE provides full coverage from

TABLE 1
STATUS OF HIGH REDSHIFT QUASAR
CANDIDATES ON STRIPE 82

Sample	Uniform	All
Candidates	92	-
... spec. ids	73	106
... quasars	71	84
... $4.7 < z < 5.1$	52	64

3100Å to $1\mu\text{m}$ at a resolution of ~ 5800 using the $0.7''$ slit. The typical seeing during this run was $0.6''$.

Magellan spectra were reduced using MASE (Bochanski et al. 2009), an IDL-based pipeline designed for MAGE data. Wavelength calibration was provided by ThAr lamps observed shortly after the targets and at a similar airmass, and the standard star Feige 110 was used for flux calibration. Of the four targets observed at Magellan, three are $z \sim 5$ quasars (Figure 20; one object had been previously observed in BOSS), and one is a star.

4.4. MMT observations

The bulk of our spectroscopic observations occurred at the MMT 6.5m telescope using the Red Channel spectrograph. We used the 270 mm^{-1} grating centered at 7500 Å^{20} , providing coverage from 5500 Å to 9700 Å . We used either the $1''$ or $1.5''$ slit based on the seeing, providing resolutions of $R \sim 640$ and $R \sim 430$, respectively.

Observations were conducted on 2011 Jun 23-24, 2011 Oct 1-4, and 2012 May 27-28. During 2011 June nine objects were observed in poor seeing ($1.5\text{--}3''$); five were confirmed as quasars. Conditions during the 2011 October run were fair with $\lesssim 1''$ seeing; however, most of the run was lost to thick clouds and high humidity, particularly during the early part of the night. As a result, we obtained few spectra for candidates at $20^{\text{h}} < \text{R.A.} < 22^{\text{h}}$. In total, 52 targets were observed in October, of which 41 were confirmed quasars. In the 2012 May run, 17 additional candidates with $20^{\text{h}} < \text{R.A.} < 24^{\text{h}}$ were observed, resulting in 11 new high-redshift quasars. Conditions during this run were excellent, with $0.7\text{--}1.2''$ seeing throughout. In general we valued efficiency over quality. Therefore the exposure times were short, between 5 and 15 minutes with typically a single exposure per target, and many of the spectra have a low signal-to-noise ratio. However, the quasars among the observed targets are easily identified by their prominent emission lines, while the few contaminants can be ruled out as high-redshift quasars by the lack of either emission lines or a strong spectral break towards blue wavelengths.

Data were processed using standard longslit reduction techniques through a combination of Pyraf²¹ and python routines, including bias subtraction, pixel level corrections from flat fields generated from internal lamps, and sky subtraction using a polynomial background fit along the slit direction. Cosmic rays were identified and masked using the LACOS routines (van Dokkum 2001). Wavelength calibration was provided from an internal HeN-

eAr lamp, and then corrected on a per-image basis using night sky lines (primarily the OH line list given by Rousselot et al. 2000). Standard stars were observed between one and three times per night and used for flux calibration. However, the conditions were highly variable and the absolute flux calibration of the spectra is not reliable. Figures 21, 22 and 23 show the MMT spectra obtained for high redshift quasars on Stripe 82.

5. QUASAR CATALOG

Table 4 consists of our full Stripe 82 $z \sim 5$ quasar catalog, consisting of:

- 11 SDSS DR7 quasars with $z \geq 4.7$,
- 14 BOSS DR9 quasars with $z \geq 4.7$,
- 59 quasars with spectra obtained at MMT and Magellan.

For all objects, we provide photometry in the *griz* bands derived from the coadded imaging that formed the basis for our target selection. We also provide *J*-band photometry obtained from our aperture photometry of the UKIDSS DR8plus images, or, when available, imaging from MMT SWIRC. The table includes all $z > 4.7$ quasars on Stripe 82 from the three data sources, but not all of these quasars are included in the uniform sample used to calculate the QLF (§6). In §6.1.2 we will derive the selection probability for each quasar, this value is included in the catalog and we flag quasars that are not part of the uniform sample by assigning them a value of -1 .

The only line widely available at a reasonable S/N in our spectra is the $\text{Ly}\alpha$ line. Our spectra do generally cover the C IV emission region; however, this line shows offsets from the systemic redshift that are correlated with properties such as luminosity and radio loudness (e.g., Richards et al. 2011). Therefore, we assign redshifts based on a combination of fitting the $\text{Ly}\alpha$ line²², measuring the onset of $\text{Ly}\alpha$ forest absorption, and visually matching a quasar template spectrum to the observed spectra. In general, the redshifts have an uncertainty of $\Delta z \sim 0.02$, which is sufficiently accurate for calculation of a luminosity function. All of our quasars are consistent with a Type I classification based on their broad line widths ($FWHM > 1000\text{ km s}^{-1}$).

We use the simulated spectra derived from our quasar model (§3.1) to derive k -corrections as a function of both redshift and luminosity. We derive the average correction for the observed *i*-band flux to the monochromatic luminosity at rest-frame 1450 Å (M_{1450}) for a large number of simulated quasars in narrow bins of (M, z) (see §6.1), then interpolate this grid to derive an individual quasar correction. Figure 6 shows the luminosity-dependent k -corrections derived from our quasar model and used in this work. Accounting for the average emission line contribution to the k -correction as a function of luminosity alleviates some of the issues arising from the fact that our best photometry is in the *i*-band, which contains the

²⁰ Some objects were observed at a redder setting during the course of a program targeting higher redshift objects.

²¹ Pyraf is a product of the Space Telescope Science Institute, which is operated by AURA for NASA.

²² The $\text{Ly}\alpha$ line can also have systematic offsets, in particular a $\sim 500\text{ km s}^{-1}$ redshift due to absorption of the blue wing by the $\text{Ly}\alpha$ forest (e.g., Shen et al. 2007). We do not account for this offset as it is much smaller than the uncertainties we assume for our redshift designations.

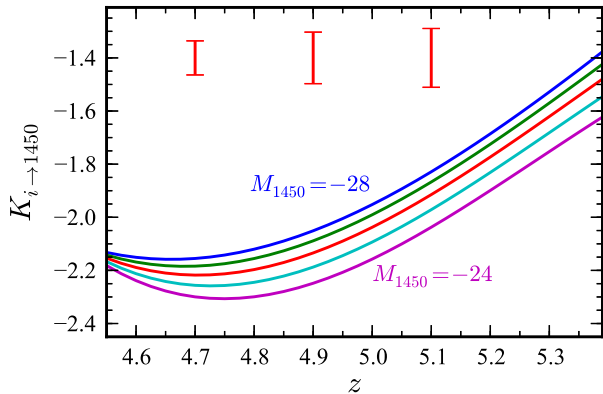


FIG. 6.— Luminosity-dependent k -correction as determined from the quasar spectral simulations. The lines show the k -correction from observed i -band magnitude to M_{1450} for $M_{1450} = -28$ (top) to $M_{1450} = -24$ (bottom), in steps of $\Delta M = 1$. The trend with redshift is fairly smooth; although $\text{Ly}\alpha$ enters the i band at $z \approx 4.6$, $\text{Ly}\alpha$ forest absorption tends to offset its effect on the k -correction. The vertical error bars at the top of the plot denote the representative scatter in the k -correction at the median luminosity ($M_{1450} = -26$) at three redshifts. This scatter is also determined from the simulations and accounts for the variations in emission line strengths, continuum shapes, and $\text{Ly}\alpha$ forest absorption included in the quasar spectral model. These corrections are from the Stripe 82 simulations; the DR7 simulations produce similar results but are adjusted for the asinh magnitude scale.

$\text{Ly}\alpha$ line.²³ This approach also corrects for some of the bias introduced by luminosity-dependent line emission and its effect on broadband photometric data. However, the distribution of intrinsic quasar SEDs at a given luminosity and redshift is quite broad, introducing scatter into our absolute magnitude calculations (also shown in Figure 6).

Alternatively, the k -correction can be derived directly from the spectral data (see, e.g., Glikman et al. 2011, for a discussion of spectral k -corrections for high- z quasars). However, we are again limited by the low S/N in the continuum of our spectra. In addition, we do not attempt an accurate flux calibration of our spectra (indeed, the BOSS quasar spectra are known to have flux calibration errors in some instances, see P aris et al. 2012). Thus we would need to calibrate the observed (noisy) spectra with the broadband fluxes from the imaging. We chose to use a template k -correction based on photometry as it can be more consistently applied.

Figure 7 shows the distribution in redshift and luminosity for both the Stripe 82 and SDSS main samples, after applying our k -corrections.

5.1. Notes on individual objects

In this section, we note objects that have radio detections, uncertain identifications from the spectroscopy, and unusual spectral features.

J221941.90+001256.2 ($z = 4.30$), **J224524.27+002414.2** ($z = 5.16$): These two objects have radio counterparts at 1.4 GHz from VLA imaging of Stripe 82 (Hodge et al. 2011). They are the only sources with counterparts in that catalog, which is derived from imaging over 92 deg² to a depth of 52 $\mu\text{Jy beam}^{-1}$. J221941.90+001256.2 has a peak flux density of $F_{1.4,\text{pk}} =$

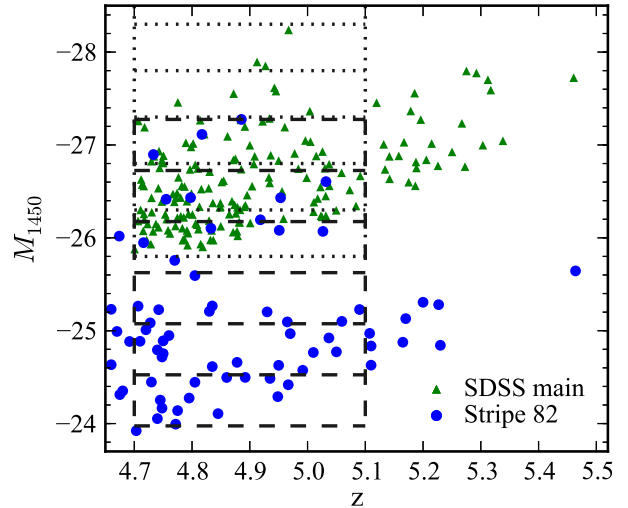


FIG. 7.— Distribution of high- z quasars in our sample in luminosity and redshift. Green triangles represent DR7 quasars, blue circles denote Stripe 82 quasars. The grid lines show the bin edges used for the calculation of the binned QLF, with dashed lines for Stripe 82 and dotted lines for DR7.

$0.92 \pm 0.07 \text{ mJy beam}^{-1}$ and **J224524.27+002414.2** has $F_{1.4,\text{pk}} = 1.09 \pm 0.06 \text{ mJy beam}^{-1}$. Both sources also have counterparts in the Faint Images of the Radio Sky at Twenty-Centimeters (FIRST) catalog (Becker et al. 1995), with peak flux densities of $F_{1.4,\text{pk}} = 0.87 \pm 0.10 \text{ mJy beam}^{-1}$ and $F_{1.4,\text{pk}} = 0.92 \pm 0.10 \text{ mJy beam}^{-1}$, respectively. Neither is included in our uniform sample as they lie outside the defined redshift range. J221941.90+001256.2 also shows strong broad absorption line (BAL) features.

J223907.56+003022.6 ($z = 5.09$), **J232741.35-002803.9** ($z = 4.75$), **J021043.16-001818.4** ($z = 5.05$): These three objects also have FIRST counterparts, with peak flux densities of $F_{1.4,\text{pk}} = 1.35 \pm 0.10 \text{ mJy beam}^{-1}$, $F_{1.4,\text{pk}} = 1.24 \pm 0.12 \text{ mJy beam}^{-1}$, and $F_{1.4,\text{pk}} = 6.82 \pm 0.10 \text{ mJy beam}^{-1}$, respectively. All three are included in the uniform sample.

J211158.01+005302.6 ($z = 4.98$), **J234730.56+002306.3** ($z = 4.71$): We identified these objects as quasars based on their discovery spectra; however, the spectra are noisy and the identifications were uncertain. We later confirmed them as quasars with MMT observations on 2012 Aug 25.

J211225.39-000141.3 ($z = 4.67$), **J030315.05-000347.6** ($z = 4.72$): These spectra also have low S/N . Both objects appear to have a Lyman break feature (more evident in the 2D spectra) and $\text{Ly}\alpha$ and N V emission features, with apparent N V absorption troughs. We include these objects as confirmed quasars. J030315.05-000347.6 may have BAL features.

J222018.48-010146.8 ($z = 5.62$), **J000552.33-000655.6** ($z = 5.86$): These two quasars were targeted as part of an SDSS+UKIDSS high- z BOSS quasar ancillary program. J000552.33-000655.6 was first reported in Fan et al. (2004).

6. RESULTS

6.1. Survey Completeness

We use the simulations described in section 3.1 to estimate the completeness of our selection criteria. To de-

²³ Note that the i -band measurement is from the coadded imaging, and is thus an average of a decade of individual measurements, smoothing over the variable lightcurve of each quasar.

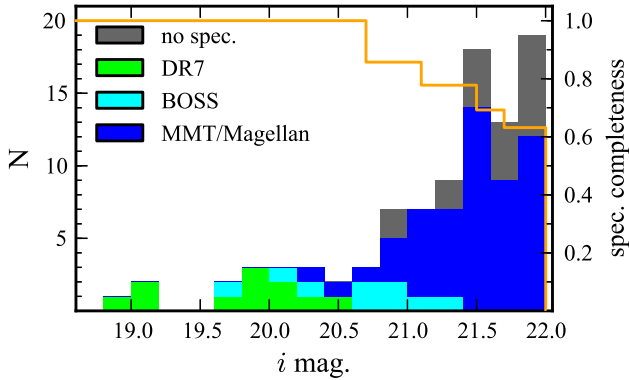


FIG. 8.— Spectroscopic completeness of $z \sim 5$ quasar candidates from the uniform sample on Stripe 82 ($i_{AB} < 22$). The histogram is divided into objects without spectroscopic observations (gray), and those with spectra obtained through DR7 (green), BOSS (cyan), and MMT/Magellan observations (blue). The orange line represents the spectroscopic incompleteness correction applied when calculating the QLF in order to account for candidates without spectra.

rive a selection function, we construct a grid of simulated quasars distributed evenly in (M_{1450}, z) space with 200 quasars per bin of $\Delta M = 0.1$, $\Delta z = 0.05$. Each object is sampled from models for quasar emission properties as outlined in § 3.1. The simulated quasars are then passed through the color cuts after adding photometric errors, and the fraction of objects within each bin that pass the cuts provides an estimate of the completeness for a given luminosity and redshift, under the assumption that our quasar model accurately represents the intrinsic distributions of quasar properties.

We generate two simulation grids. The first adopts photometric uncertainties typical of the SDSS main survey and uses asinh magnitudes; we use this simulation to derive the completeness of the SDSS quasar survey at $z \sim 5$. The second uses photometric uncertainties from the coadded imaging and is used for the Stripe 82 sample. The uncertainties are determined by fitting a relation to the uncertainties of stellar objects in the Stripe 82 catalog as a function of band flux.

6.1.1. DR7 Completeness

The SDSS quasar selection algorithm (Richards et al. 2002) was not finalized until the survey was already in progress, thus to construct a statistical sample from DR7 we follow the method given in Richards et al. (2006) to identify DR7 quasars from regions with uniform target selection. This limits the final area to 6222 deg^2 . We further cut the DR7 sample to only objects selected by the *riz* color inclusion regions (excluding objects selected only as *griz* stellar locus outliers); this results in the loss of only a few objects, but greatly simplifies the calculation of the selection function. After restricting to the uniform targeting area and applying the color cuts, DR7QSO provides 146 quasars with $4.7 < z < 5.1$ ²⁴.

We use the simulated quasar photometry combined with the *riz* color cuts of Richards et al. (2002) to derive the selection function for $z \sim 5$ quasars in the main SDSS sample (Figure 9). We add a 5% correction for photomet-

ric incompleteness (i.e., objects lost due to crowding or proximity to bright stars or galaxies, see Richards et al. 2006) and spectroscopic incompleteness of 5% (objects selected by the targeting algorithm but without a spectrum in DR7). We determined the latter incompleteness by querying the DR7 Target database for objects with the QSO_HIZ flag, finding that 5% lack spectra. The missing spectra are mainly due to fiber collisions that result when tiling spectroscopic targets, due to the restriction that fibers on a single plate must be separated by $> 55''$.

6.1.2. Stripe 82 Completeness

Although the Stripe 82 selection function is obtained from the same quasar model as for DR7, it is evident from Figure 9 that the Stripe 82 selection probes a different population. First, the Stripe 82 data are much deeper and thus the completeness remains high to lower luminosities. Also, the color selection criteria are somewhat different. Figure 10 compares the selection efficiencies for DR7 and Stripe 82 as a function of redshift. It is noteworthy that the selection function value is higher for fainter objects at some redshifts. This is because the selection function calculation averages over a range of colors in each (M, z) bin, with the colors depending on the continuum slopes, line strengths, and other features sampled from the model. At $z \sim 5$, our color selection is very sensitive to the Ly α equivalent width, as shown in Figure 11. Because the EW increases at lower luminosities and Ly α is fully within the *i*-band in our redshift range, the colors of fainter objects are redder in *r* – *i* and bluer in *i* – *z* than brighter objects, increasing their likelihood of meeting our selection criteria (see also Figure 5). This effect is not captured by models that do not account for the Baldwin Effect.

We estimate the photometric completeness to be 95% (see, e.g., Fig. 7 of Annis et al. 2011). The spectroscopic coverage of the Stripe 82 candidates is high: $\sim 90\%$ of candidates with $i_{AB} < 21.5$ have spectra. Near the faint limit, the completeness is a bit lower: 69% of candidates with $21.5 < i_{AB} < 21.7$ and 63% of candidates with $21.7 < i_{AB} < 22$ have spectra. Figure 8 shows our spectroscopic completeness as a function of observed magnitude, as well as the correction we use to account for the missing spectra in our luminosity function calculation. In total, 19 candidates do not have spectroscopic identifications; by applying this correction we assume that they are a random subsample of the full candidate set. This assumption is fair given that the choice of which targets to observe was largely constrained by sky location and weather conditions, not properties of the candidates themselves (such as color).

The Stripe 82 survey includes 52 quasars at $4.7 < z < 5.1$. The Stripe 82 sample is not only highly complete but also highly pure: out of 73 candidates with spectroscopic identifications, 71 are high-redshift quasars ($z > 4$), and 52 (71%) are quasars in the targeted redshift range. For completeness, we provide in Table 5 a list of the candidates that were either not observed spectroscopically (19 objects), or were found not to be high-redshift quasars (2 objects, both have no emission features and appear to be stellar continua).

6.2. Binned Luminosity Function

²⁴ We do not double-count DR7 quasars that lie on Stripe 82 when calculating the LF, as the uniform targeting area does not include Stripe 82.

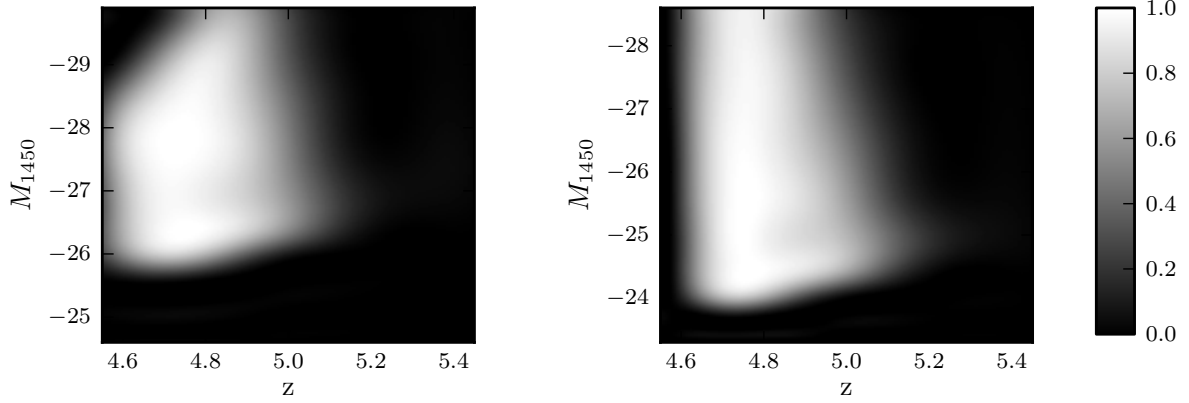


FIG. 9.— Selection functions for the SDSS main sample (left, $i_{\text{asinh}} < 20.2$) and Stripe 82 (right, $i_{\text{AB}} < 22$). Note the difference in scale on the y -axis, as the Stripe 82 survey reaches nearly two magnitudes fainter than the SDSS main. The selection probability is calculated in each (M, z) bin by determining the fraction of the 200 simulated quasars in each bin that pass the selection criteria, averaging over the SED distribution.

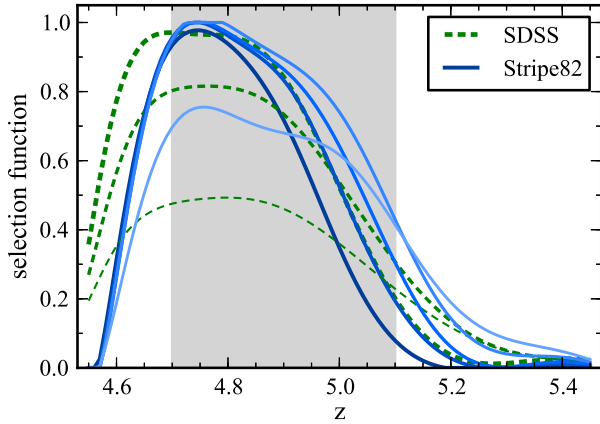


FIG. 10.— Comparison of the selection functions for the SDSS main sample (green) and Stripe 82 (blue). The lines represent slices at fixed observed magnitude through the functions shown in Figure 9. For the SDSS main, the slices are at $i_{\text{asinh}} = (19.1, 20, 20.2)$, and for Stripe 82 they are at $i_{\text{AB}} = (19.1, 20.2, 21, 21.5, 21.9)$. The lines become thinner and lighter with increasing magnitude. We restrict our uniform sample to $4.7 < z < 5.1$ where the completeness is highest (gray shaded region). Although the completeness is relatively high at $z \sim 4.65$, the selection function is steep here, which would make incompleteness corrections very sensitive to systematics in the selection function model.

We first calculate the luminosity function from the combined SDSS main and Stripe 82 $z \sim 5$ quasar samples by dividing the sample into discrete bins of luminosity and redshift. Guided by our completeness calculations, we restrict the sample to the interval $4.7 < z < 5.1$, where the selection efficiency is relatively high. We refer to this as the uniform sample. We use a single redshift bin, ignoring any evolution of the QLF parameters over the width of the bin. In particular, the redshift evolution derived by Fan et al. (2001b) predicts a decline by a factor of ~ 1.5 in space density from $z = 4.7$ to $z = 5.1$. We do not account for this evolution in the binned QLF, but it will be incorporated below in a maximum likelihood fit to each quasar. We calculate the binned luminosity function using the $1/V_a$ method (Schmidt 1968; Avni & Bahcall 1980), including the correction of Page & Carrera (2000). The calculation is performed separately on the DR7 and Stripe 82 data, accounting for the differences in sky area, depth, and selection criteria between the two samples.

Table 2 provides the binned QLF for both the SDSS

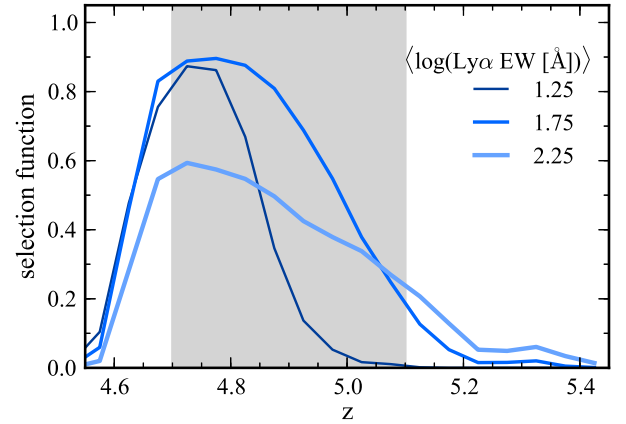


FIG. 11.— Dependence of the Stripe 82 selection function value derived from the simulations on the $\text{Ly}\alpha$ equivalent width. The simulated quasars are divided into three bins of $\text{Ly}\alpha$ EW, with median values shown on the plot. The anticorrelation between EW and luminosity means that objects with greater $\text{Ly}\alpha$ EW are fainter on average, and thus have a lower selection probability. On the other hand, the $\text{Ly}\alpha$ line itself introduces redshift-dependent trends. For example, objects at $z \gtrsim 5$ with strong $\text{Ly}\alpha$ emission will have redder $r - i$ and bluer $i - z$ colors, and thus be more likely to pass our selection criteria. This effect is apparent in Fig. 5, which shows that lower luminosity sources fall within the color selection criteria over a wider redshift range than higher luminosity sources.

main (DR7) and Stripe 82 samples. We include the number counts in each magnitude bin, as well as the corrected number counts after accounting for all sources of incompleteness. The binned QLF data is also displayed in Figure 12. The SDSS data show a steep drop in the number density at the bright end; from the combined data it is evident that the QLF becomes shallower towards lower luminosities. Fitting a single power law to the binned data from both surveys at the bright end ($M_{1450} < -27.0$) results in a steep slope of $\beta = -3.7$.

Shen & Kelly (2012) have also calculated the binned QLF of SDSS quasars at $z = 4.75$, repeating the DR3 analysis of Richards et al. (2006) for the larger DR7 sample. Our methodology differs from that of Shen & Kelly (2012) in several respects. Most notably, we have recalculated the selection function and k -corrections using our new quasar model. In addition, we restrict the quasar sample to color-selected objects (excluding those identified only as stellar locus outliers). The Richards et al.

TABLE 2
BINNED QLF

M_{1450}	N	N_{cor}	$\log \Phi^a$	σ_Φ^b
DR7				
-28.05	3	4.8	-9.45	0.21
-27.55	5	7.7	-9.24	0.26
-27.05	30	42.0	-8.51	0.58
-26.55	57	85.1	-8.20	0.92
-26.05	51	81.5	-7.90	1.89
Stripe 82				
-27.00	2	2.2	-8.40	2.81
-26.45	5	8.1	-7.84	6.97
-25.90	5	7.0	-7.90	5.92
-25.35	10	16.7	-7.53	10.23
-24.80	15	24.3	-7.36	11.51
-24.25	14	26.8	-7.14	19.90

^a Φ is in units of $\text{Mpc}^{-3} \text{mag}^{-1}$.^b σ_Φ is in units of $10^{-9} \text{Mpc}^{-3} \text{mag}^{-1}$.

(2006) selection function has a value of ~ 1 at $z \gtrsim 5$, much higher than the values we obtain (see Fig. 10), and inconsistent with our previous finding (§6.1.1) that few quasars were selected by locus outlier criteria alone. However, although our selection function disagrees with that of Richards et al. (2006) by as much as a factor of ~ 2 at $z \sim 5$, the highest redshift bin ($4.5 < z < 5.0$) in both Richards et al. (2006) and Shen & Kelly (2012) is dominated by objects near the low redshift edge of the bin. Finally, we use a slightly different method for calculating the spatial area of the survey; however, we obtain a similar result (6222 deg^2 vs. 6248 deg^2). Figure 12 compares our binned QLF to Richards et al. (2006) and Shen & Kelly (2012); the agreement is generally good, though differences of $\sim 20\text{--}30\%$ may still be attributed to the different approaches used.

6.3. Parameter Estimation From Maximum Likelihood

We now derive parametric fits to the observed data using maximum likelihood estimation. The maximum likelihood estimate for a luminosity function $\Phi(M, z)$ corresponds to the minimum of the log likelihood function

$$S = -2 \sum_i^N \ln[\Phi(M_i, z_i)] + 2 \int \int \Phi(M, z) p(M, z) \frac{dV}{dz} dM dz,$$

where the first sum is over the observed quasars, and the second is over the full luminosity and redshift range of the sample and provides the normalization (Marshall et al. 1983, see Fan et al. 2001a and Kelly et al. 2008 for alternative derivations of the likelihood function). The term $p(M, z)$ is the probability that a quasar with absolute magnitude M (for our purposes, M_{1450}) and redshift z is included in the survey; i.e., the selection function as derived in section 6.1, including all sources of incompleteness. Confidence intervals are derived from the likelihood function using a χ^2 distribution in $\Delta S = S - S_{\text{min}}$ (Lampton et al. 1976).

Over a wide redshift range, the quasar luminosity function is found to be well fit by a double power law (Boyle et al. 1988),

$$\Phi(M, z) = \frac{\Phi^*(z)}{10^{0.4(\alpha+1)(M-M^*)} + 10^{0.4(\beta+1)(M-M^*)}},$$

where M^* is the characteristic luminosity at which the

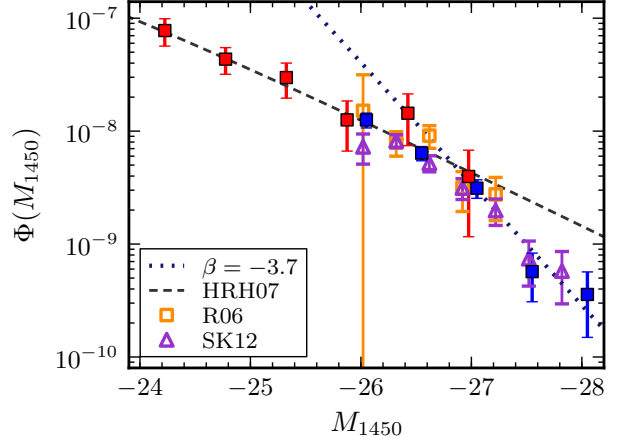


FIG. 12.— Binned QLF at $\langle z \rangle = 4.9$ from SDSS main (blue) and Stripe 82 (red). The dotted line shows a single power law fit to points with $M_{1450} < -27.0$ ($\beta = -3.7$). The departure from a single power law is evident when the faint Stripe 82 data are included. For comparison, we show previous calculations of the binned QLF at $z = 4.75$, corrected for our cosmology and shifted to $z = 4.9$ using the redshift evolution from Fan et al. (2001b). The orange points represent the SDSS DR3 calculation from an area of 1622 deg^2 (Richards et al. 2006), while the purple points show the SDSS DR7 calculation from Shen & Kelly (2012) using a sample nearly identical to our SDSS main sample covering $\sim 6200 \text{ deg}^2$. The dashed lines correspond to the Hopkins et al. (2007b) QLF model discussed in §6.4; most of the constraint on this model at $z = 5$ comes from the Richards et al. (2006) points.

function changes slope from steep at the bright end (β) to shallow at the faint end (α). The four QLF parameters may evolve with redshift, possibly in an interdependent manner. Given the limited redshift range of our survey, we will only account for the steep decline in number density at high redshift using the fit of Fan et al. (2001b): $\Phi^*(z) = \Phi^*(z = 6) \times 10^{k(z-6)}$, with $k = -0.47$.²⁵

Even with a sample of nearly 200 quasars spanning $\Delta M \approx 4$, there are substantial degeneracies in fitting the data with this parameterization. In particular, while the departure from a single power law form towards faint luminosities is clear from the binned data, the faint end slope itself is not well constrained. This results in considerable freedom in the placement of the break luminosity. We thus perform several fits while fixing one or more parameters.

Table 3 shows the results of several model fits with various choices for the fixed parameters, including uncertainties derived by varying a single parameter and calculating the likelihood for the best-fit solution for the other parameters. First, we compare fits with different fixed values for the faint end slope. Surveys of faint $z \lesssim 3$ quasars typically find $\alpha = -1.5$ (Hunt et al. 2004; Richards et al. 2005; Siana et al. 2008; Croom et al. 2009), while observations at high redshift favor a steeper value of $\alpha = -1.7$ (Glikman et al. 2010; Ikeda et al. 2011; Masters et al. 2012), albeit with large uncertainties due to the difficulties of assembling large samples of faint quasars at high redshift. The model fits in Table 3 are compared to the binned QLF in Figure 13.

We find that the steeper value for the faint end slope is marginally favored by our data, but at only the $\sim 33\%$ confidence level. The $\alpha = -1.7$ fit has a higher break

²⁵ We normalize Φ^* to $z = 6$ for easier comparison to the higher redshift results.

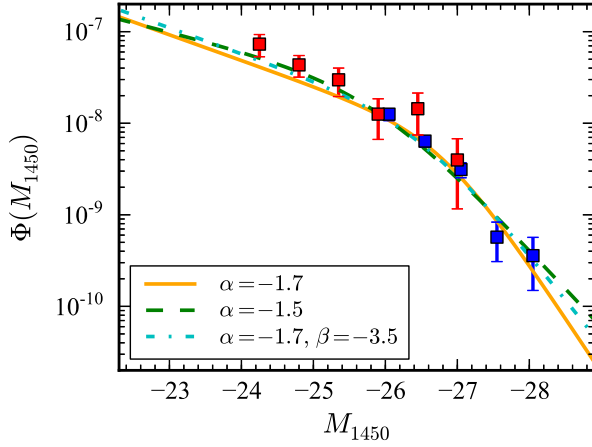


FIG. 13.— The double power law fits from maximum likelihood analysis (Table 3) plotted against the binned QLF data. Each model fit is labeled by the choice of fixed parameters for that fit.

TABLE 3
MLE FIT PARAMETERS

$\log \Phi^*(z=6)$	M_{1450}^*	α	β	ΔS	$P(\chi^2)$
$-8.62^{+0.49}_{-0.22}$	$-26.81^{+0.90}_{-0.38}$	-1.70	$-3.98^{+0.96}_{-1.55}$		
$-8.10^{+0.50}_{-0.37}$	$-25.88^{+1.02}_{-0.72}$	-1.50	$-3.12^{+0.40}_{-0.73}$	3.40	0.33
$-8.46^{+0.18}_{-0.17}$	$-26.53^{+0.29}_{-0.30}$	-1.70	-3.50	0.38	0.83
$-8.40^{+0.05}_{-0.05}$	-26.39	-1.80	-3.26	0.40	0.52

NOTE. — Parameters without uncertainty ranges are fixed during the maximum likelihood fitting. The last two columns give the confidence level for the best-fit model (first row) compared to various alternative choices for the fixed parameters, in terms of $\Delta S = S - S_{\min}$, which follows a χ^2 distribution.

^a $\log \Phi^*(z) = \log \Phi^*(z=6) + k(z-6)$, with $k = -0.47$.

luminosity ($M_{1450}^* = -26.8$) and steeper bright end slope ($\beta = -4.0$) compared to the $\alpha = -1.5$ fit ($M_{1450}^* = -25.9$, $\beta = -3.1$). We further explore the parameter degeneracies by calculating the joint likelihood ranges for β and M_{1450}^* for the two fixed values of the faint end slope, as shown in Figure 14. For $\alpha = -1.7$, we derive 95% confidence intervals of $\beta < -2.67$ and $27.35 < M_{1450}^* < -24.87$; for $\alpha = -1.5$, we derive 95% confidence intervals of $\beta < -2.51$ and $-26.94 < M_{1450}^* < -23.48$. The strong constraints on the steepness of the bright end slope show that a flattening of the bright end slope at high redshift, as found by, e.g., Richards et al. (2006), is not in agreement with our data. This is likely due to the fact that Richards et al. (2006) fit a single power law slope to the SDSS data under the assumption that the break luminosity was well below their flux limit; we will discuss this further in the following section.

6.4. Evolution of the QLF

We provide some context for these fits by comparing to results at lower and higher redshift. Ross et al. (2012) recently presented a QLF measurement at $2.2 < z < 3.5$ from the BOSS DR9 quasar sample. Over this redshift range, the QLF is well-fit by a Luminosity Evolution and Density Evolution (LEDE) model, where the power law slopes have fixed values and the normalization and break

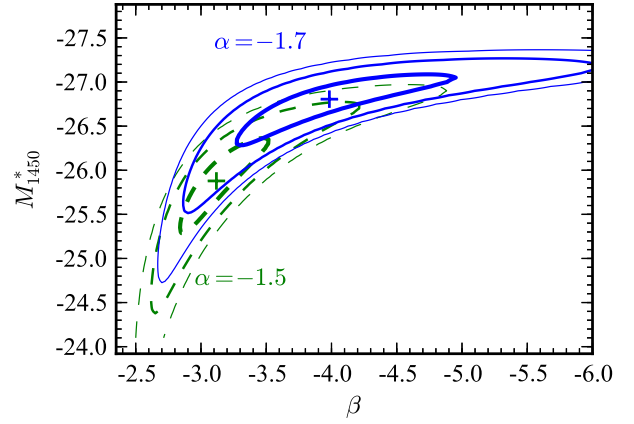


FIG. 14.— Likelihood contours for β and M_{1450}^* , for two different (fixed) values for the faint-end slope α . Contours are drawn at the 68%, 95%, and 99.6% confidence intervals, with decreasing line thickness. The best-fit values for each parameter are indicated with a cross.

luminosity evolve in a log-linear fashion. Specifically,

$$\log[\Phi^*(z)] = \log[\Phi^*(z=2.2)] + c_1(z-2.2), \quad (1)$$

$$M_{i,2}^*(z) = M_{i,2}^*(z=2.2) + c_2(z-2.2). \quad (2)$$

In equation 2, $M_{i,2} \equiv M_i(z=2) = M_{1450} - 1.486$ is the absolute i -band magnitude at $z=2$ (Richards et al. 2006), corresponding to rest-frame $\sim 2600\text{\AA}$ and assuming a spectral index of $\alpha_\nu = -0.5$ ($f_\nu \propto \nu^\alpha$). The evolution in M^* and Φ^* implied by this model is shown in Figure 15, extrapolated to higher redshift to compare to our data. While evolution in the power law slopes is not well constrained by the data, our results are consistent with the values obtained from the BOSS data, with some indication that the faint end slope steepens toward higher redshift [from Ross et al. 2012, $\alpha(2.2 < z < 3.5) = -1.42^{+0.51}_{-0.01}$ and $\beta(2.2 < z < 3.5) = -3.53^{+0.09}_{-0.29}$]. To further facilitate comparison to the BOSS results, we include a fit with the bright end slope fixed to $\beta = -3.5$ while retaining a steeper faint end slope of $\alpha = -1.7$. This choice of slopes results in a fit that is fully consistent with our best fit (the χ^2 indicates this model can only be ruled out when compared to the best-fit model at the 17% confidence level). However, the values for M^* and Φ^* do not agree with the simple extrapolation of the LEDE model from lower redshift. This can be clearly seen in Figure 16, which shows the LEDE prediction at $z = 4.9$ significantly overestimates our measurements. We will discuss a modified form to the LEDE model that provides a better fit to the high redshift evolution in §6.6.

At higher redshift, we compare to the $z \sim 6$ QLF measurement reported by Willott et al. (2010). Table 3 shows a fit where all the parameters except Φ^* have been fixed to the best-fit values from Willott et al. (2010) for a fixed faint end slope of $\alpha = -1.8$ (we use this value as it provides a better fit to our data than their $\alpha = -1.5$ fit). This model differs from our best-fit model by a likelihood of $\Delta S = 0.4$ and is disfavored at only the 48% confidence level. Thus the shape of our QLF at $z \sim 5$ is consistent with the current best measurements at $z \sim 6$. However, the normalization is quite different: it is a factor of ~ 1.6 higher than predicted by evolving the Willott et al. (2010) model to $z = 4.9$ us-

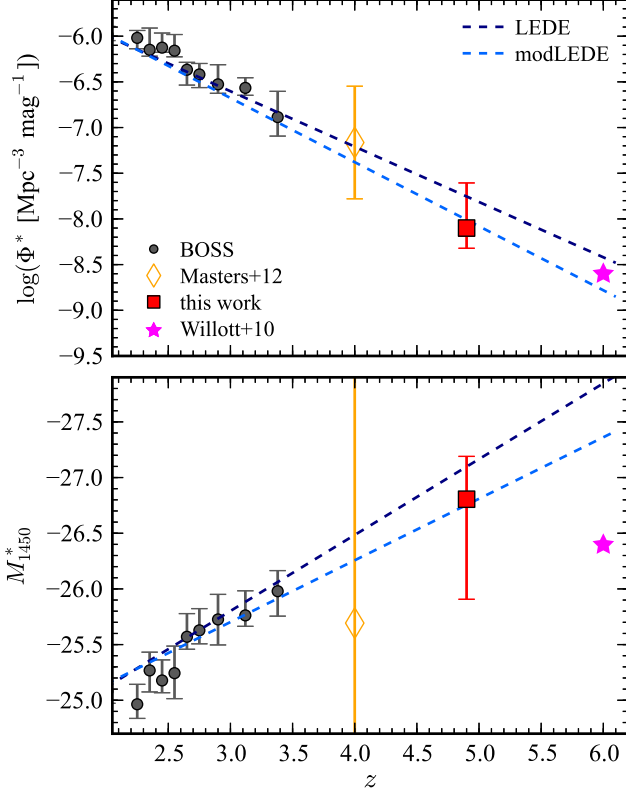


FIG. 15.— Evolution of the QLF normalization (Φ^*) and break luminosity (M_{1450}^*) between $z \sim 2$ and $z \sim 5$. The points at $2.2 < z < 3.5$ come from the BOSS DR9 QLF (Ross et al. 2012), using a sample of ~ 6000 variability-selected quasars from Stripe 82. The point at $z = 4.9$ is from the best-fit model in Table 3. The point at $z = 4$ is from Masters et al. (2012) and the one at $z = 6$ is from Willott et al. (2010), using their $\alpha = -1.8$ fit (uncertainties for the parameters were not reported for this fit). All points have been corrected to match our cosmology. The log-linear LEDE model fit to the BOSS data is shown as a dark blue dashed line; the modified form of this model discussed in §6.6 is shown as a light blue dashed line.

ing $k = -0.47$, as they adopted for their fit (they obtained $\log \Phi^*(z = 6) = -8.6$, in contrast to the value of $\log \Phi^*(z = 6) = -8.4$ we obtain when fitting the shape of their QLF to our $z = 5$ data). Figure 16 illustrates the discrepancy in the normalization from the evolved Willott et al. (2010) model; we will discuss this point further in § 6.6.

The empirical QLF model of Hopkins et al. (2007b, hereafter HRH07) combines observations in the optical, X-ray, and mid-infrared bands to construct a bolometric QLF from $z = 0$ to $z = 5$. At high redshift the most constraining data in HRH07 comes from optical surveys, which have shown a flattening of the bright end slope at high redshift (Schmidt et al. 1995; Fan et al. 2001b; Richards et al. 2006). In the HRH07 model, the break luminosity increases with redshift until $z \sim 2$ and then turns over, such that it is a factor of ~ 10 lower luminosity at $z = 5$ than at $z = 2$, contrary to our finding that the break luminosity increases monotonically to $z \sim 5$. At $z = 5$, the HRH07 model predicts a quite low break luminosity ($M_{1450}^* \sim -22.6$) and a shallow bright end slope ($\beta \sim -2.5$). Figure 12 shows that the HRH07 model agrees with our data at $-27 < M_{1450} < -26$, which is not surprising since at $z \sim 5$ their fit is mainly to the Richards et al. (2006)

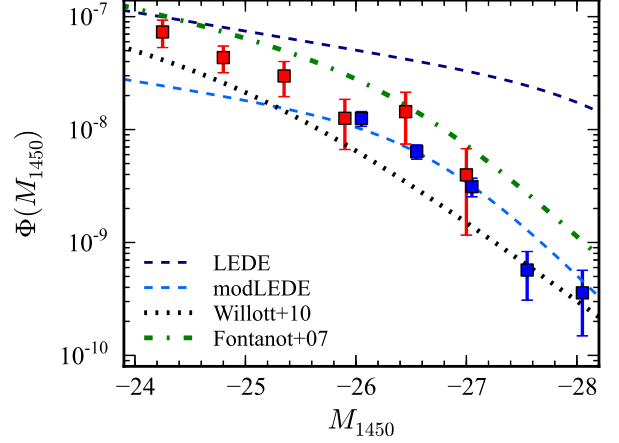


FIG. 16.— Evolutionary models for the QLF plotted against our binned data at $z = 4.9$. The dark and light blue dashed lines are the BOSS LEDE and modified LEDE forms, respectively, as in Fig. 15. The LEDE model clearly disagrees with the data; the modified form agrees with the bright end reasonably well. The black dotted line represents the fit at $z = 6$ from Willott et al. (2010) shifted to $z = 4.9$ using the Fan et al. (2001b) redshift evolution; the shape is roughly similar to our data but it clearly underestimates the normalization. The green dot-dashed line represents the QLF fit from Fontanot et al. (2007).

data. The agreement at lower luminosities is likely a coincidence due to the faint-end slope being shallow (and similar to their bright-end slope). However, the HRH07 model clearly fails to match the shape at the bright end, which we attribute to a steeper slope and a much brighter M_{1450}^* . This demonstrates the substantial degeneracies in the QLF parameters, as the HRH07 values for Φ^* and M_{1450}^* at $z = 5$ would not even appear on Figure 15, even though the model itself provides a good fit to our data at $M_{1450} \gtrsim -27$. The key difference between our work and HRH07 (and by extension, Richards et al. 2006) is the increased survey area at the bright end, which is needed to extend *above* the break luminosity at this redshift and make the break in the luminosity function more evident.

Finally, we examine the $z = 5$ QLF from (Fontanot et al. 2007). This work combines bright quasars from SDSS DR3 with faint quasars from the *Great Observatories Origins Deep Survey* (GOODS; Dickinson et al. 2003) over the redshift range $3.5 < z < 5.2$. Figure 16 compares their pure density evolution (PDE) model (#12 from their Table 3) to our data. We find that the Fontanot et al. (2007) model overestimates our QLF measurements at all luminosities, possibly due to the completeness correction they applied (see also Ikeda et al. 2012).

In conclusion, we find tentative evidence for a mild steepening of the faint-end slope, and no evidence in favor of an evolution in the bright end slope, although both of these parameters are poorly constrained at most redshifts. On the other hand, we do see evidence for strong evolution in the break luminosity, as it brightens from $M_{1450}^* \approx -25.4$ at $z = 2.5$ to $M_{1450}^* \approx -26.8$ at $z = 5$ (Figure 15). This evolution has consequences for surveys where the faint limit is near the break luminosity, as single power law fits to such data would naturally find a flatter slope. The problem is evident in Figure 12, which shows that a single power law can describe the SDSS DR3 data from Richards et al. (2006), the full range of which is near the break luminosity. The possibility that

high redshift fits to the bright end of the QLF may be biased by a higher break luminosity was put forward by Assef et al. (2011) and Shen & Kelly (2012). Based on our fits at $z = 5$ and the greater dynamic range of our survey, we find this scenario to be plausible; i.e., the flattening of the bright end slope at high redshift reported previously (Schmidt et al. 1995; Fan et al. 2001b; Richards et al. 2006; Hopkins et al. 2007b) may be attributed instead to rapid evolution in the break luminosity.

6.5. Comparison to Theoretical Predictions

Figure 17 compares our data to various theoretical models for the QLF at $z = 5$. Shen (2009) provides a theoretical prediction for the evolution of the QLF in a cosmological framework by relating the growth of SMBHs to the hierarchical assembly of their host dark matter halos. In this model, quasar activity is triggered by major mergers of halos. Their fiducial model reproduces the observed QLF at $0.5 < z < 4.5$, but underpredicts the observed QLF at higher redshifts. Indeed, their fiducial model lies below our data at $z = 5$ (Figure 17). Shen (2009) also has a variant of this fiducial model that includes a faster redshift evolution in the normalization of the scaling relation between peak quasar luminosity and host halo mass, a redshift evolution in the scatter of this relation and an increase in the upper host halo mass above which quasar triggering is cut off exponentially in order to better fit the QLF at higher redshifts (see Sec. 4.4 of Shen 2009, for details). This alternative model provides a good fit to our data at the bright end, but overpredicts the number counts at the faint end.

Conroy & White (2012) introduce a model in which quasars are tied to galaxies in a straightforward manner through the $M_{\text{BH}} - M_{\text{gal}}$ relation, so that the evolution of the QLF is determined by the evolution of this relation. Their model includes two free parameters that are allowed to vary with redshift: the quasar duty cycle and the normalization of the $M_{\text{BH}} - M_{\text{gal}}$ relation. Conroy & White (2012) constrain these parameters from existing QLF measurements at $0.5 < z < 4.75$. The high redshift constraints mainly come from the SDSS (Richards et al. 2006) and have limited dynamic range, leading to significant uncertainties in the $z \sim 5$ prediction (represented by the gray shaded region in Figure 17, see also Fig. 3 in Conroy & White 2012). Overall, the Conroy & White (2012) model provides a good fit to the data.

DeGraf et al. (2010) present a QLF prediction based on hydrodynamic simulations that include radiative cooling, star formation, black holes, and feedback processes. This work has since been updated to a larger simulation volume, with $100 h^{-1}$ Mpc on a side and 2×1792^3 particles (DeGraf et al, in prep.). At each timestep, the QLF is calculated from the active black holes, and the final QLF prediction is derived by time-averaging the individual measurements. This allows the bright end of the QLF to be estimated by catching the brief episodes of peak luminosity among the rare, massive black hole population. Figure 17 shows the prediction of this model in our redshift range, including an estimate for cosmic variance derived by comparing two simulation volumes (represented by the extent of the shaded region). This model generally agrees with our data near and just below the break

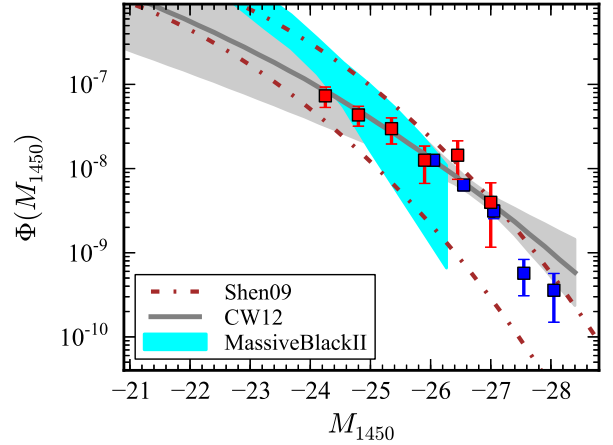


FIG. 17.— Comparison of observed QLF to various theoretical predictions. The two models of Shen (2009) are shown as dashed brown lines; the lower line is their fiducial model, and the upper line is their modified model as described in the text. The model of Conroy & White (2012) is represented by a solid gray line, with the shaded region indicating the 1σ uncertainty range. The range of the predicted QLF from the “MassiveBlackII” hydrodynamic simulations is represented by the cyan shaded region.

luminosity. It appears to be somewhat steeper than the data at faint luminosities, though fainter measurements of the QLF from deeper optical data or at other wavelengths (e.g., X-rays) are needed to better constrain the model.

We remind the reader that our QLF only accounts for unobscured, Type I quasars. Our measurements are lower limits on the true density of actively accreting black holes, assuming some fraction are in an obscured (or even mildly extinguished) growth phase. For example, comparison to X-ray surveys indicates that only $\sim 25\%$ of quasars are unobscured at $z = 4$ (Masters et al. 2012). Some inconsistency with theoretical models that do not distinguish between unobscured and obscured quasars is thus expected.

6.6. Spatial Density of Luminous Quasars

A rapid decline in the comoving number density of quasars at high redshift was observed three decades ago (Osmer 1982). Following Fan et al. (2001a), we quantify this evolution in terms of the spatial density of quasars above a minimum luminosity within a redshift window. The density is derived from the $1/V_a$ method, where for each quasar the volume within which it would have been observed within a survey is

$$V_a = \int_{\Delta z} p(M_{1450}, z) \frac{dV}{dz} dz,$$

where $p(M, z)$ is again the selection function for the survey. From this equation, the total spatial density and its uncertainty are estimated by

$$\rho = \sum_i \frac{1}{V_a^i}, \quad \sigma(\rho) = \left[\sum_i \left(\frac{1}{V_a^i} \right)^2 \right]^{1/2},$$

where the sum is over all quasars more luminous than M . This density is related to the luminosity function in that

$$\rho(< M, z) = \int_{-\infty}^M \Phi(M, z) dM, \quad (3)$$

where $\rho(< M, z)$ is the space density of quasars more luminous than M . We choose to perform a sum over our data rather than an integration over the QLF as the latter requires extrapolation and model fitting. We calculate this quantity at $z \sim 4$, $z \sim 5$, and $z \sim 6$, combining data from SDSS, our work, and multiple surveys at $z \sim 6$. We choose a limit of $M_{1450} = -26$ as it corresponds to the lowest luminosity quasars in the SDSS sample at $z \sim 4$.

At $z = 4.25$ we use the uniform quasar sample from the SDSS DR7 described in §6.1.1. This sample includes 311 quasars with $4.1 < z < 4.4$, representing a factor of four increase in number over the SDSS DR3 results given in Richards et al. (2006). We adopt the selection function given in Table 1 of that work rather than recalculate it from our simulations, as the SDSS quasar target selection has a complicated dependence on the extent of the stellar locus in color space (Richards et al. 2002), which is captured by the Richards et al. (2006) selection function. At $z = 4.9$ we use our combined sample from the SDSS DR7 and from Stripe 82 and the selection functions presented in section 6.1. Finally, at $z = 6$ we use the sample compiled by Willott et al. (2010), consisting of quasars from the SDSS main (Fan et al. 2001a, 2003, 2004, 2006b), SDSS deep (Jiang et al. 2008, 2009), and CFHTQS (Willott et al. 2010). We derive selection functions for the three $z \sim 6$ quasar surveys using our quasar simulations, extended to higher redshift. The derived selection functions from our models agree well with those shown in Figure 4 of Willott et al. (2010).

Figure 18 shows the evolution of the space density of luminous quasars ($M_{1450} < -26$) from $z = 4$ to $z = 6$. Our measurement at $z = 5$ shows a decline in the space density by a factor of 1.8 from $z = 4.25$. Fan et al. (2001b) fit an exponential decline to the space density at high redshifts, finding that $\rho(M_{1450} < -25.5, z) \sim 10^{kz}$ with $k = -0.47$ at $z > 3.6$, about a factor of three per unit redshift. Brusa et al. (2009) reported a similar value ($k = -0.43$) using X-ray-selected quasars at $z \sim 3.0$ – 4.5 ($\log L_X > 44.2$). Our results from $z = 4.25$ to $z = 5$ are in good agreement with these results; we measure a decline of 2.4 ± 0.3 per unit redshift ($k = -0.38$).

On the other hand, the evolution to $z = 6$ is more pronounced: a factor of 5.1 ± 1.5 per unit redshift ($k = -0.7$), or roughly twice the rate measured at lower redshift (Figure 18). The departure of the $z = 6$ measurement from the prediction based on the slope fit to the $4 \lesssim z \lesssim 5$ data is significant at the 4.5σ level. If we integrate deeper for the two high redshift bins, to a limit of $M_{1450} < -24.5$, the decline is even stronger. We obtain $\rho(M_{1450} < -24.5, z = 4.9) = 4.2 \pm 0.7 \times 10^{-8} \text{ Mpc}^{-3}$ and $\rho(M_{1450} < -24.5, z = 6.0) = 0.5 \pm 0.1 \times 10^{-8} \text{ Mpc}^{-3}$, corresponding to a factor of 6.5 ± 1.7 decline per unit redshift.

We check the consistency of our faint-end measurements by comparing to recent work at X-ray wavelengths with the *Chandra*-COSMOS survey (Civano et al. 2011), which is sensitive to moderate-luminosity ($\log L_{(2-10 \text{ keV})} > 44.15 \text{ erg s}^{-1}$) AGN at $z \sim 5$. In order to compare the two samples, we must integrate our double power law model to $M_{1450} = -24.0$ (adopting the α_{ox} relation from Young et al. 2010). Civano et al. (2011) identified three X-ray-selected Type

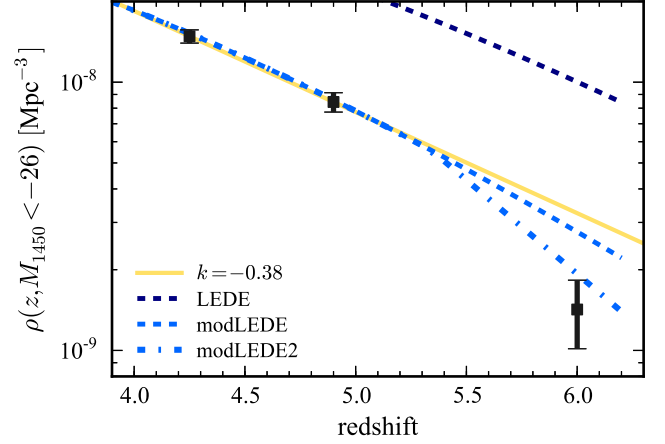


FIG. 18.— Evolution of the number density of luminous quasars at high redshift. The data are described in §6.6. The yellow solid line shows the slope derived from a log-linear fit to the $z = 4$ and $z = 5$ points [$\log \rho(z) \propto -0.38z$], a value that is similar to the Fan et al. (2001b) result based on 39 bright quasars at $3.6 < z < 5$ from early Stripe 82 data. The $z = 6$ point is well below this trend, departing from it at 4.5σ . From $z = 5$ to $z = 6$ the number density declines as $\log \rho(z) = -0.7z$. The upper dark blue dashed line shows the extrapolated LEDE QLF model from the BOSS DR9, which clearly overpredicts the high redshift number densities. We modify the LEDE model to have a steeper evolution in $\log \Phi^*$ and shallower evolution in M_{1450}^* with redshift (light blue dashed line, see details in text), and further impose a maximum break luminosity of $M_{1450}^* > -27$ (light blue dot-dashed line).

I quasars in the redshift bin $4.2 < z < 5.4$, which translates to an observed space density of $\Phi(4.2 < z < 5.4) = (2.5 \pm 1.5) \times 10^{-7} \text{ Mpc}^{-3}$. Integrating our best-fit model for the QLF over that redshift bin, we obtain $\Phi(4.2 < z < 5.4) = 0.8 \times 10^{-7} \text{ Mpc}^{-3}$. Thus our QLF agrees with the Civano et al. (2011) results to within the $\sim 1\sigma$ uncertainties, especially when considering that to make the comparison we must extrapolate our QLF in both luminosity and redshift. The X-ray data do not strongly constrain the evolution to $z \sim 6$ due to the small area of the *Chandra*-COSMOS survey (from zero $z \sim 6$ objects in Civano et al. 2011, the decline from $z = 5$ to $z = 6$ is > 2 per unit redshift).

We now relate the decline in the high-redshift quasar density to the evolutionary model for the QLF derived from the BOSS DR9 (Ross et al. 2012). In this LEDE model, $\log \Phi^*$ declines by 0.6 dex per unit redshift, while M^* brightens by 0.68 mag per unit redshift ($c_1 = -0.6$ in equation 1 and $c_2 = -0.68$ in equation 2, respectively). Integrating this model (equation 3) shows that it significantly overpredicts the high redshift number densities we have derived (Figure 18). This result suggests that the steeper decline in the high-redshift number counts begins at $z \lesssim 4$, and is also consistent with Figure 15, which shows that the $\log \Phi^*$ predicted by the LEDE model is higher than the data at $z \gtrsim 5$, and is not well constrained at $z \sim 4$. We thus modify the LEDE model from BOSS by steepening the slope of the $\log \Phi^*(z)$ evolution to $c_1 = -0.7$, and softening the slope of the M_{1450}^* evolution to $c_2 = -0.55$. These modifications are within the 1σ uncertainties of the values derived from fitting BOSS data; Figure 18 shows that they bring the QLF model in agreement with the integral constraints from the $z \sim 4$ – 5 data, but not the $z = 6$ point. At $z = 4.9$,

this modified evolutionary model predicts $M_{1450}^* = -26.8$ and $\log \Phi^* = -8.0$. This provides a good match to the values we obtained when fixing the slopes to the BOSS values during the MLE fit, $M_{1450}^* = -26.6$ and $\log \Phi^*(z = 4.9) = -7.9$ (Table 3).

Finally, we consider further modifying the model for the evolution of M^* . It is unlikely that M^* continues to rise to very high luminosities; indeed, Figure 15 shows that the high-redshift fits for M^* are somewhat below the LEDE prediction. We thus impose a maximum break luminosity of $M_{1450}^* = -27$, which in the modified LEDE model is reached at $z \sim 5.4$. This choice causes a turnover in the high-redshift number densities that matches the data at $z \sim 6$ (Figure 18). This model is somewhat arbitrary, but qualitatively, a model in which Φ^* has a more rapid downward evolution at high redshift and M^* brightens until $z \sim 4-5$ and then levels off (or even turns over) provides a reasonable description of the high redshift data. A quasar with $M_{1450}^* = -27$ radiating at the Eddington luminosity corresponds to a $\sim 2 \times 10^9 M_\odot$ black hole; it seems reasonable to suppose that while the break luminosity evolves strongly at high redshift, it would not greatly exceed this value.

6.7. Contribution of $z \sim 5$ quasars to the ionizing background

The number of ionizing photons required to maintain hydrogen ionization as a function of redshift can be found by balancing the ionizing photon emissivity with the density of hydrogen and the rate of recombinations. The recombination rate depends on the clumping factor, $C = \langle n_H^2 \rangle / \langle n_H \rangle^2$. Madau et al. (1999) present an equation for the ionizing photon density \dot{N}_{ion} that adopts a high value for the clumping factor ($C = 30$). More recent work suggests that the clumping factor is not so large; Meiksin (2005) argues that $C \approx 5$ and McQuinn et al. (2011) use cosmological simulations that include the effects of Lyman-limit systems and find $C \approx 2-3$ at $z = 6$.

We calculate the ionizing photon output for each quasar by assuming a broken power-law SED with an index of $\alpha_\nu = -1.7$ at ultraviolet wavelengths (Telfer et al. 2002), a break at 1100Å, and an index of $\alpha_\nu = -0.5$ above the break. Rescaling the Madau et al. (1999) equation and updating to our cosmology, we estimate the number of photons required to maintain full ionization at $z = 5$ to be $\dot{N}_{\text{ion}} = 3.4 \times 10^{50} (C/5) \text{ Mpc}^{-3} \text{ s}^{-1}$. Integrating the QLF model fits to $M_{1450}^* = -20$ gives $\dot{N}_Q \sim 6 \times 10^{49} \text{ Mpc}^{-3} \text{ s}^{-1}$, or $\approx 17\%$ of the number required (this number depends only weakly on which model fit is used). For $C = 2$, quasars provide $\sim 40\%$ of the photons required for hydrogen ionization, suggesting they may have played some role in maintaining ionization at $z \sim 5$. However, the steeper decline of luminous quasars from $z \sim 5$ to $z \sim 6$ further reduces the likelihood that quasars were an important source of ionizing photons during the reionization epoch. Indeed, even when assuming a steep faint-end slope ($\alpha = -1.8$), Willott et al. (2010) find that $z \sim 6$ quasars generate $< 10\%$ of the required ionizing photon background. This is also in good agreement with constraints from deep X-ray surveys (Barger et al. 2003; Fontanot et al. 2007) that limit the contribution from moderate luminosity AGN at $z > 6$.

7. CONCLUSIONS

This work builds on the legacy of SDSS Stripe 82 for high-redshift quasar studies. Fan et al. (2004) first used coadded photometry from ~ 5 epochs of Stripe 82 imaging to discover a single $z \sim 6$ quasar with $z_{\text{AB}} = 20.5$, fainter than the limit adopted for the single-epoch imaging. Subsequently, Jiang et al. (2008, 2009) created deep, coadded images from the 50–60 epochs available at the completion of SDSS I/II to discover 11 quasars at $z > 5.8$ to a limit of $z_{\text{AB}} = 22.8$. In this work, we have utilized the bluer SDSS bands to conduct a survey of $z \sim 5$ quasars, a redshift where current constraints on the QLF are relatively weak.

We define a sample of 92 candidates to a limit of $i_{\text{AB}} = 22.0$ using color selection criteria and with a well-defined selection function. From this sample, 73 objects have spectroscopic observations, and 71 are confirmed high redshift quasars. We then focus on the redshift range $4.7 < z < 5.1$ where our completeness is highest. Using a sample of 52 quasars from our work on Stripe 82 combined with 146 bright quasars from the SDSS DR7, we calculate the optical quasar luminosity function at $z = 5$.

We have fit a double power law model to our observational data at $z = 5$, and reach the following conclusions:

- There is no clear evidence for evolution in the shape of the QLF from $z \sim 2$ to $z \sim 6$. We find a steep bright-end slope ($\beta \sim -3.5$, Fig. 12) that roughly agrees with measurements at both lower (e.g., BOSS $2.2 < z < 3.5$, Ross et al. 2012) and higher ($z = 6$, Willott et al. 2010; Jiang et al. 2009) redshifts. A relatively steep value for the faint end slope is favored ($\alpha \sim -1.7$) in agreement with other high redshift results, but the faint end is not strongly constrained by our data.
- We see the break in the luminosity function in our $z \sim 5$ data, finding that $M_{1450}^*(z = 4.9) = -26.8_{-0.4}^{+0.9}$ for $\alpha = -1.7$ (Fig. 14). The strong covariances between the power law slopes and the break luminosity lead to significant uncertainties in these quantities, but the best fit value for the break luminosity is higher than at $z = 3.4$, where the BOSS results find $M_{1450}^*(z = 3.4) = -26.0 \pm 0.2$.
- The decline in the space density of luminous quasars at high redshift is greater than indicated by previous surveys. We find that while the decline in the integrated space density of quasars with $M_{1450} < -26$ from $z \sim 4$ to $z \sim 5$ is about a factor of three per unit redshift, in agreement with previous results, the decline to $z \sim 6$ is nearly a factor of two greater (Fig. 18). This suggests a much more rapid dropoff in luminous quasar activity at the highest redshifts currently probed by observations.
- By comparing to a simple LEDE model for the redshift evolution of BOSS quasars, we find that in addition to the steeper decline in number density, there is also an indication that the brightening of the break luminosity with redshift does not continue indefinitely. A toy model in which the evolution of Φ^* is somewhat steeper than from a simple

extrapolation from the BOSS data, and in which the break luminosity evolves somewhat more slowly and peaks at $M_{1450}^* = -27$, provides a good match to the high redshift data.

- Our model for the QLF at $z \sim 5$ predicts that quasars contribute ~ 20 – 50% of the ionizing photons required to maintain hydrogen ionization at this redshift, with the uncertainty dominated by our lack of understanding of the clumping factor.

The strong evolution in the high redshift quasar number density we have found has implications for quasar surveys at even higher redshifts. Early forecasts for UKIDSS anticipated roughly 10 $z \sim 7$ quasars from the survey (Warren & Hewett 2002), much greater than the one found to date (Mortlock et al. 2011) from over half the survey area. Using a redshift evolution of $\log \rho \propto -0.47z$ (Fan et al. 2001b), extrapolation of our QLF predicts that there are ~ 9 quasars at $6.5 < z < 7.5$ in the UKIDSS DR8plus release to a limit of $Y = 19.6$ (based on Fig. 7 of Mortlock et al. 2012). The shallower QLF measured at $z = 6$ by Willott et al. (2010) predicts ~ 6 quasars. Based on our results, these estimates should be revised downward to ~ 6 and ~ 3 , respectively. Assuming the selection efficiency is $\lesssim 50\%$, this brings the predicted number counts closer to the actual observations. Further, the decline may continue to steepen at $z > 6$, so that the lower yield from UKIDSS may be due in part to an even stronger downward evolution with redshift.

Significant progress has been made over the last decade in measuring the evolution of the high redshift quasar population. Nonetheless, the observations are not yet strongly constraining of models that make, for example, different predictions for the evolution of the power law slopes. Ongoing high redshift quasar surveys will improve these constraints. We are currently extending our work to fainter luminosities at $z \sim 5$ using deeper optical imaging data, obtaining improved measurements of the faint end slope and break luminosity. We will also use Stripe 82 data to measure the QLF at $z \sim 4$ over a wide range of luminosities. Finally, Pan-STARRS

(Kaiser et al. 2002) is obtaining shallow optical and near-infrared imaging, including the y -band, over an area of sky over that is more than twice that of the SDSS. To date, one $z \sim 6$ quasar has been discovered from this survey (Morganson et al. 2012); future work should reduce the uncertainty on the bright end of the QLF at $z \sim 6$ and better constrain the strong evolution we have measured from existing data.

8. ACKNOWLEDGEMENTS

The authors thank the staffs of the MMT and Magellan telescopes, particularly the recently retired John McAfee, for enabling many of the observations presented here. IDM, LJ and XF acknowledge support from a David and Lucile Packard Fellowship, and NSF Grants AST 08-06861 and AST 11-07682.

Funding for SDSS-III has been provided by the Alfred P. Sloan Foundation, the Participating Institutions, the National Science Foundation, and the U.S. Department of Energy Office of Science. The SDSS-III web site is <http://www.sdss3.org/>.

SDSS-III is managed by the Astrophysical Research Consortium for the Participating Institutions of the SDSS-III Collaboration including the University of Arizona, the Brazilian Participation Group, Brookhaven National Laboratory, University of Cambridge, Carnegie Mellon University, University of Florida, the French Participation Group, the German Participation Group, Harvard University, the Instituto de Astrofísica de Canarias, the Michigan State/Notre Dame/JINA Participation Group, Johns Hopkins University, Lawrence Berkeley National Laboratory, Max Planck Institute for Astrophysics, Max Planck Institute for Extraterrestrial Physics, New Mexico State University, New York University, Ohio State University, Pennsylvania State University, University of Portsmouth, Princeton University, the Spanish Participation Group, University of Tokyo, University of Utah, Vanderbilt University, University of Virginia, University of Washington, and Yale University.

Facilities: MMT (Red Channel spectrograph, SWIRC), Magellan:Clay (MAGE), SDSS

REFERENCES

- Abazajian, K. N., Adelman-McCarthy, J. K., Agüeros, M. A., et al. 2009, *ApJS*, 182, 543
- Ahn, C. P., Alexandroff, R., Allende Prieto, C., et al. 2012, *ApJS*, 203, 21
- Aihara, H., Allende Prieto, C., An, D., et al. 2011, *ApJS*, 193, 29
- Annis, J., Soares-Santos, M., Strauss, M. A., et al. 2011, *ArXiv e-prints*, 1111.6619
- Assef, R. J., Kochanek, C. S., Ashby, M. L. N., et al. 2011, *ApJ*, 728, 56
- Avni, Y., & Bahcall, J. N. 1980, *ApJ*, 235, 694
- Baldwin, J. A. 1977, *ApJ*, 214, 679
- Barger, A. J., Cowie, L. L., Capak, P., et al. 2003, *ApJ*, 584, L61
- Becker, R. H., White, R. L., & Helfand, D. J. 1995, *ApJ*, 450, 559
- Bertin, E., & Arnouts, S. 1996, *AJ*, 117, 393
- Bertin, E., Mellier, Y., Radovich, M., et al. 2002, in *Astronomical Society of the Pacific Conference Series*, Vol. 281, *Astronomical Data Analysis Software and Systems XI*, ed. D. A. Bohlender, D. Durand, & T. H. Handley, 228
- Bochanski, J. J., Hennawi, J. F., Simcoe, R. A., et al. 2009, *PASP*, 121, 1409
- Bolton, A. S., Schlegel, D. J., Aubourg, E., et al. 2012, *ApJ*
- Bolton, J. S., Oh, S. P., & Furlanetto, S. R. 2009, *MNRAS*, 395, 736
- Bovy, J., Hennawi, J. F., Hogg, D. W., et al. 2011, *ApJ*, 729, 141
- Boyle, B. J., Shanks, T., Croom, S. M., et al. 2000, *MNRAS*, 317, 1014
- Boyle, B. J., Shanks, T., & Peterson, B. A. 1988, *Monthly Notices of the Royal Astronomical Society* (ISSN 0035-8711), 235, 935
- Brotherton, M. S., Tran, H. D., Becker, R. H., et al. 2001, *ApJ*, 546, 775
- Brown, W. R., McLeod, B. A., Geary, J. C., & Bowsher, E. C. 2008, in *Society of Photo-Optical Instrumentation Engineers (SPIE) Conference Series*, Vol. 7014, *Society of Photo-Optical Instrumentation Engineers (SPIE) Conference Series*
- Brusa, M., Comastri, A., Gilli, R., et al. 2009, *ApJ*, 693, 8
- Carlberg, R. G. 1990, *ApJ*, 350, 505
- Casali, M., Adamson, A., Alves de Oliveira, C., et al. 2007, *A & A*, 467, 777
- Cattaneo, A., Haehnelt, M. G., & Rees, M. J. 1999, *MNRAS*, 308, 77
- Chiu, K., Zheng, W., Schneider, D. P., et al. 2005, *AJ*, 130, 13
- Civano, F., Brusa, M., Comastri, A., et al. 2011, *ApJ*, 741, 91
- Conroy, C., & White, M. 2012, *ArXiv e-prints*, 1208.3198
- Cowie, L. L., Barger, A. J., Bautz, M. W., Brandt, W. N., & Garmire, G. P. 2003, *ApJ*, 584, L57

- Croom, S. M., Richards, G. T., Shanks, T., et al. 2009, MNRAS, 399, 1755
- Dawson, K. S., Schlegel, D. J., Ahn, C. P., et al. 2012, ApJ
- Degraf, C., Di Matteo, T., & Springel, V. 2010, MNRAS, 402, 1927
- Di Matteo, T., Khandai, N., DeGraf, C., et al. 2012, ApJ, 745, L29
- Di Matteo, T., Springel, V., & Hernquist, L. 2005, ApJ, 433, 604
- Diamond-Stanic, A. M., Fan, X., Brandt, W. N., et al. 2009, AJ, 699, 782
- Dickinson, M., Giavalisco, M., & GOODS Team. 2003, in *The Mass of Galaxies at Low and High Redshift*, ed. R. Bender & A. Renzini, 324, arXiv:astro-ph/0204213
- Dijkstra, M., Haiman, Z., & Loeb, A. 2004, ApJ, 613, 646
- Eisenstein, D. J., Weinberg, D. H., Agol, E., et al. 2011, ApJ, 142, 72
- Fan, X. 1999, AJ, 117, 2528
- Fan, X., Hennawi, J. F., Richards, G. T., et al. 2004, AJ, 128, 515
- Fan, X., Narayanan, V. K., Lupton, R. H., et al. 2001a, AJ, 122, 2833
- Fan, X., Strauss, M. A., Becker, R. H., et al. 2006a, AJ, 132, 117
- Fan, X., Strauss, M. A., Richards, G. T., et al. 2006b, AJ, 131, 1203
- Fan, X., Strauss, M. A., Schneider, D. P., et al. 1999, AJ, 118, 1
- . 2001b, AJ, 121, 54
- . 2003, AJ, 125, 1649
- Fontanot, F., Cristiani, S., Monaco, P., et al. 2007, A&A, 461, 39, arXiv:astro-ph/0608664
- Frieman, J. A., Bassett, B., Becker, A., et al. 2007, AJ, 135, 338
- Fukugita, M., Ichikawa, T., Gunn, J. E., et al. 1996, AJ, 111, 1748
- Gaskell, C. M. 1982, ApJ, 263, 79
- Glikman, E., Bogosavljević, M., Djorgovski, S. G., et al. 2010, ApJ, 710, 1498
- Glikman, E., Djorgovski, S. G., Stern, D., et al. 2011, ApJL, 728, L26
- Gunn, J. E., Carr, M., Rockosi, C., et al. 1998, AJ, 116, 3040
- Gunn, J. E., Siegmund, W. A., Mannery, E. J., et al. 2006, AJ, 131, 2332
- Haiman, Z., & Loeb, A. 1998, ApJ, 503, 505
- Hambly, N. C., Collins, R. S., Cross, N. J. G., et al. 2008, MNRAS, 384, 637
- Hasinger, G., Miyaji, T., & Schmidt, M. 2005, A & A, 441, 417
- Hernquist, L. 1989, ApJ, 340, 687
- Hewett, P. C., Warren, S. J., Leggett, S. K., & Hodgkin, S. T. 2006, MNRAS, 367, 454
- Hodge, J. A., Becker, R. H., White, R. L., Richards, G. T., & Zeimann, G. R. 2011, AJ, 142, 3
- Hodgkin, S. T., Irwin, M. J., Hewett, P. C., & Warren, S. J. 2009, MNRAS, 394, 675
- Hogg, D. W., Finkbeiner, D. P., Schlegel, D. J., & Gunn, J. E. 2001, AJ, 122, 2129
- Hopkins, P. F., Hernquist, L., Cox, T. J., et al. 2005, ApJ, 630, 716
- . 2006, ApJS, 163, 1
- Hopkins, P. F., Lidz, A., Hernquist, L., et al. 2007a, ApJ, 662, 110
- Hopkins, P. F., Richards, G. T., & Hernquist, L. 2007b, ApJ, 654, 731
- Huff, E. M., Hirata, C. M., Mandelbaum, R., et al. 2011, ArXiv e-prints, 1111.6958
- Hunt, M. P., Steidel, C. C., Adelberger, K. L., & Shapley, A. E. 2004, ApJ, 605, 625
- Ikedo, H., Nagao, T., Matsuoka, K., et al. 2011, ApJL, 728, L25
- Ikedo, H., Nagao, T., Matsuoka, K., et al. 2012, ApJ, 756, 160, 1207.1515
- Ivezić, Ž., Lupton, R. H., Schlegel, D., et al. 2004, AJ, 325, 583
- Jiang, L., Fan, X., Annis, J., et al. 2008, AJ, 135, 1057
- Jiang, L., Fan, X., Bian, F., et al. 2009, AJ, 138, 305
- Jiang, L., Fan, X., Hines, D. C., et al. 2006, AJ, 132, 2127
- Kaiser, N., Aussel, H., Burke, B. E., et al. 2002, in *Society of Photo-Optical Instrumentation Engineers (SPIE) Conference Series*, Vol. 4836, Society of Photo-Optical Instrumentation Engineers (SPIE) Conference Series, ed. J. A. Tyson & S. Wolff, 154–164
- Kauffmann, G., & Haehnelt, M. 2000, MNRAS, 311, 576
- Kelly, B. C., Fan, X., & Vestergaard, M. 2008, ApJ, 682, 874
- Kirkpatrick, J. A., Schlegel, D. J., Ross, N. P., et al. 2011, ApJ, 743, 125
- Komatsu, E., Dunkley, J., Nolte, M. R., et al. 2009, ApJS, 180, 330
- Kuhn, O., Elvis, M., Bechtold, J., & Elston, R. 2001, ApJS, 136, 225
- Lampton, M., Margon, B., & Bowyer, S. 1976, ApJ, 208, 177
- Lawrence, A., Warren, S. J., Almaini, O., et al. 2007, MNRAS, 379, 1599
- Lupton, R. H., Gunn, J. E., & Szalay, A. S. 1999, AJ, 118, 1406
- Madau, P., Haardt, F., & Rees, M. J. 1999, ApJ, 514, 648
- Marshall, H. L., Tananbaum, H., Avni, Y., & Zamorani, G. 1983, ApJ, 269, 35
- Marshall, J. L., Burles, S., Thompson, I. B., et al. 2008, in *Ground-based and Airborne Instrumentation for Astronomy II (SPIE)*, 701454–701454–10
- Masters, D., Capak, P., Salvato, M., et al. 2012, ApJ, 755, 169
- McDonald, P., & Eisenstein, D. 2007, ApJ, 76, 063009
- McQuinn, M. 2012, MNRAS, 426, 1349
- McQuinn, M., Oh, S. P., & Faucher-Giguère, C.-A. 2011, ApJ, 743, 82
- Meiksin, A. 2005, MNRAS, 356, 596
- Miralda-Escudé, J., Haehnelt, M., & Rees, M. J. 2000, ApJ, 530, 1
- Morganson, E., De Rosa, G., Decarli, R., et al. 2012, AJ, 143, 142
- Mortlock, D. J., Patel, M., Warren, S. J., et al. 2012, MNRAS, 419, 390
- Mortlock, D. J., Warren, S. J., Venemans, B. P., et al. 2011, Nature, 474, 616
- Oke, J. B., & Gunn, J. E. 1983, AJ, 266, 713
- Osmer, P. S. 1982, ApJ, 253, 28
- Padmanabhan, N., Schlegel, D. J., Finkbeiner, D. P., et al. 2008, AJ, 674, 1217
- Page, M. J., & Carrera, F. J. 2000, MNRAS, 311, 433
- Palanque-Delabrouille, N., Magneville, C., Yèche, C., et al. 2012, ArXiv e-prints, 1209.3968
- Palanque-Delabrouille, N., Yèche, C., Myers, A. D., et al. 2011, A & A, 530, 122
- Pâris, I., Petitjean, P., Aubourg, É., et al. 2012, A & A, 548, 66
- Pei, Y. C. 1995, ApJ, 438, 623
- Reichard, T. A., Richards, G. T., Schneider, D. P., et al. 2003, AJ, 125, 1711
- Richards, G. T., Croom, S. M., Anderson, S. F., et al. 2005, MNRAS, 360, 839
- Richards, G. T., Fan, X., Newberg, H. J., et al. 2002, AJ, 123, 2945
- Richards, G. T., Fan, X., Schneider, D. P., et al. 2001, AJ, 121, 2308
- Richards, G. T., Kruczek, N. E., Gallagher, S. C., et al. 2011, AJ, 141, 167
- Richards, G. T., Strauss, M. A., Fan, X., et al. 2006, AJ, 131, 2766
- Ross, N. P., McGreer, I. D., White, M., et al. 2012, ArXiv e-prints, 1210.6389
- Ross, N. P., Myers, A. D., Sheldon, E. S., et al. 2012, ApJS, 199, 3
- Rousselot, P., Lidman, C., Cuby, J.-G., Moreels, G., & Monnet, G. 2000, A & A, 354, 1134
- Salpeter, E. E. 1964, ApJ, 140, 796
- Scannapieco, E., Silk, J., & Bouwens, R. 2005, ApJ, 635, L13
- Schlegel, D. J., Finkbeiner, D. P., & Davis, M. 1998, AJ, 500, 525
- Schmidt, M. 1968, AJ, 151, 393
- Schmidt, M., Schneider, D. P., & Gunn, J. E. 1995, AJ, 110, 68
- Schneider, D. P., Richards, G. T., Hall, P. B., et al. 2010, AJ, 139, 2360
- Schneider, D. P., Schmidt, M., & Gunn, J. E. 1991, *Astronomical Journal* (ISSN 0004-6256), 102, 837
- Shen, Y. 2009, ApJ, 704, 89
- Shen, Y., & Kelly, B. C. 2012, ApJ, 746, 169
- Shen, Y., Strauss, M. A., Oguri, M., et al. 2007, AJ, 133, 2222
- Siana, B., Polletta, M. d. C., Smith, H. E., et al. 2008, ApJ, 675, 49
- Smee, S., Gunn, J. E., Uomoto, A., et al. 2012, ArXiv e-prints, 1208.2233
- Songaila, A. 2004, AJ, 127, 2598
- Songaila, A., & Cowie, L. L. 2010, ApJ, 721, 1448
- Stoughton, C., Lupton, R. H., Bernardi, M., et al. 2002, AJ, 123, 485
- Telfer, R. C., Zheng, W., Kriss, G. A., & Davidsen, A. F. 2002, ApJ, 565, 773

- Ueda, Y., Akiyama, M., Ohta, K., & Miyaji, T. 2003, *AJ*, 598, 886
- van Dokkum, P. G. 2001, *PASP*, 113, 1420,
arXiv:astro-ph/0108003
- Vanden Berk, D. E., Schneider, D. P., Richards, G. T., et al. 2005, *AJ*, 129, 2047
- Vestergaard, M., & Wilkes, B. J. 2001, *ApJS*, 134, 1
- Volonteri, M. 2010, *The Astronomy and Astrophysics Review*, 18, 279
- Warren, S., & Hewett, P. 2002, in *Astronomical Society of the Pacific Conference Series*, Vol. 283, *A New Era in Cosmology*, ed. N. Metcalfe & T. Shanks, 369, arXiv:astro-ph/0201216
- Warren, S. J., Hewett, P. C., & Osmer, P. S. 1994, *ApJ*, 421, 412
- Weymann, R. J., Morris, S. L., Foltz, C. B., & Hewett, P. C. 1991, *ApJ*, 373, 23
- Willott, C. J., Delfosse, X., Forveille, T., Delorme, P., & Gwyn, S. D. J. 2005, *ApJ*, 633, 630
- Willott, C. J., Delorme, P., Reyl  , C., et al. 2010, *AJ*, 139, 906
- Worseck, G., & Prochaska, J. X. 2011, *ApJ*, 728, 23
- Wyithe, J. S. B., & Loeb, A. 2003, *ApJ*, 595, 614
- Yip, C. W., Connolly, A. J., Vanden Berk, D. E., et al. 2004, *AJ*, 128, 2603
- York, D. G., Adelman, J., Anderson Jr, J. E., et al. 2000, *AJ*, 120, 1579
- Young, M., Elvis, M., & Risaliti, G. 2010, *ApJ*, 708, 1388

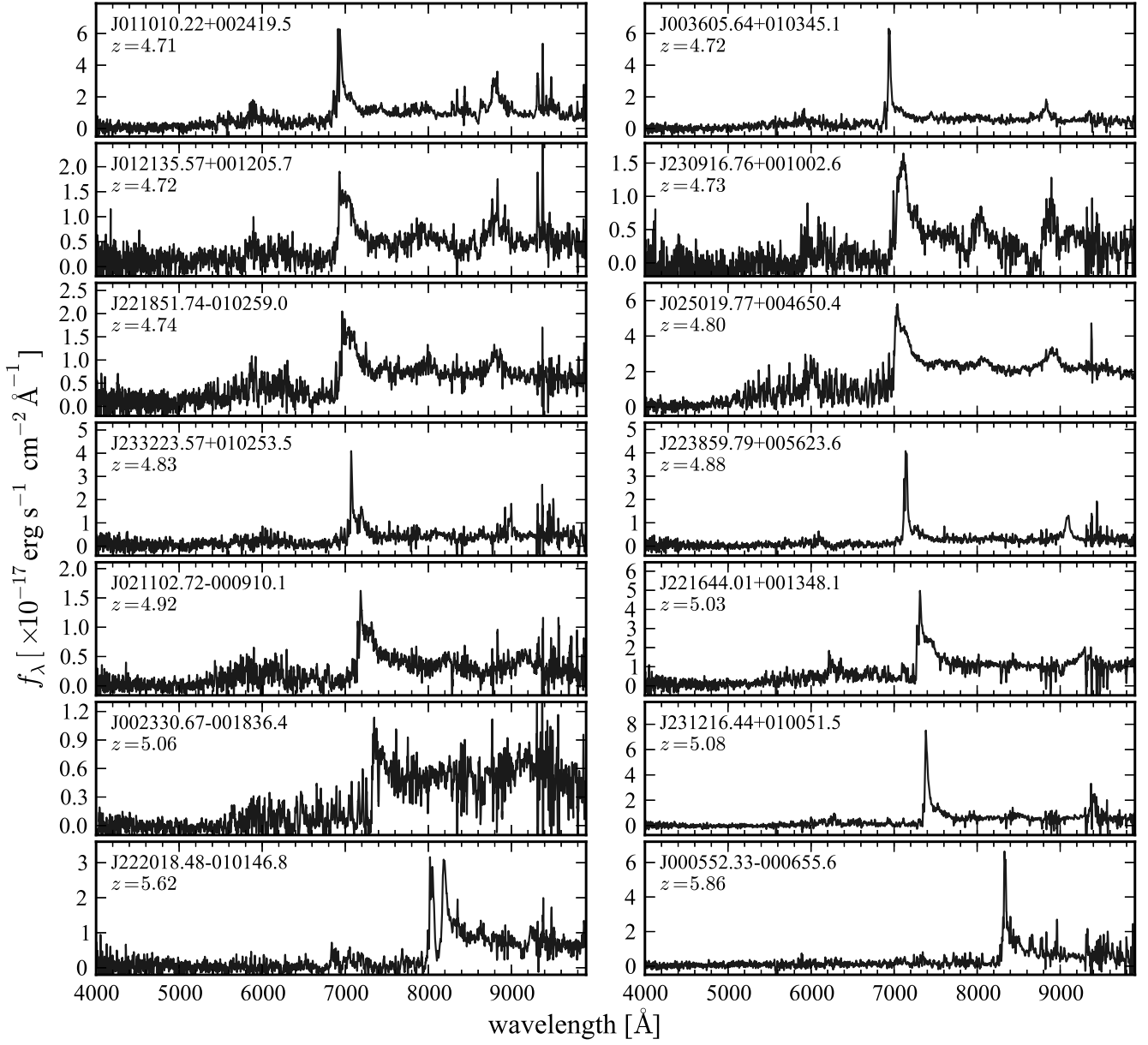


FIG. 19.— Spectra of $z > 4.7$ Stripe 82 quasars from BOSS, smoothed with a 5 pixel boxcar. In addition to the coordinates and redshift, each plot gives the plate-MJD-fiber designation for the BOSS observation.

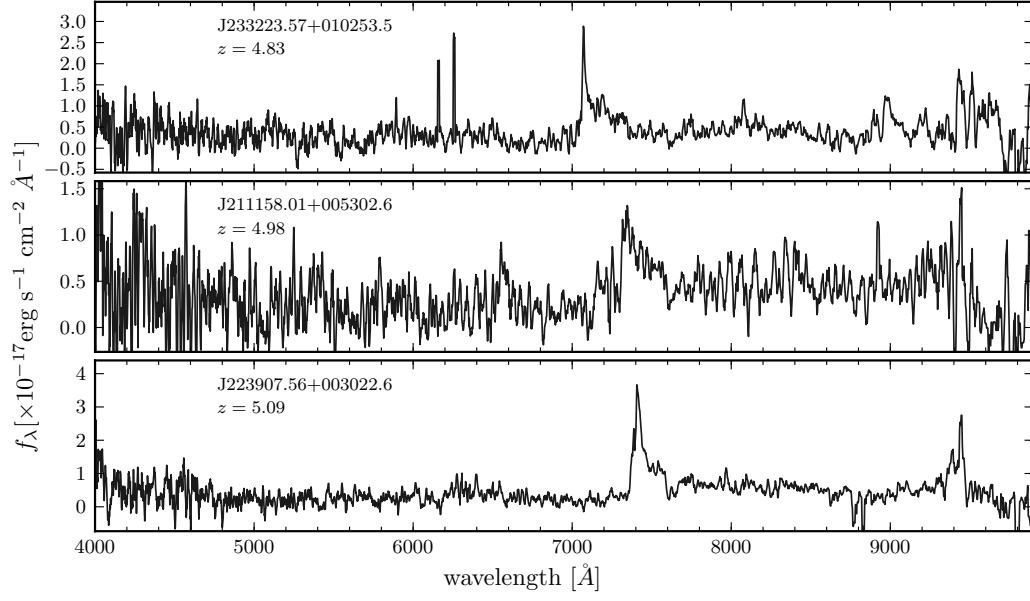


FIG. 20.— Spectra of Stripe 82 quasars observed with Magellan. The spectra have been rebinned to a resolution of $R \approx 1200$ and then smoothed with a 5 pixel ($\sim 10 \text{ \AA}$) boxcar. The first object is a repeat observation of an object with a BOSS spectrum.

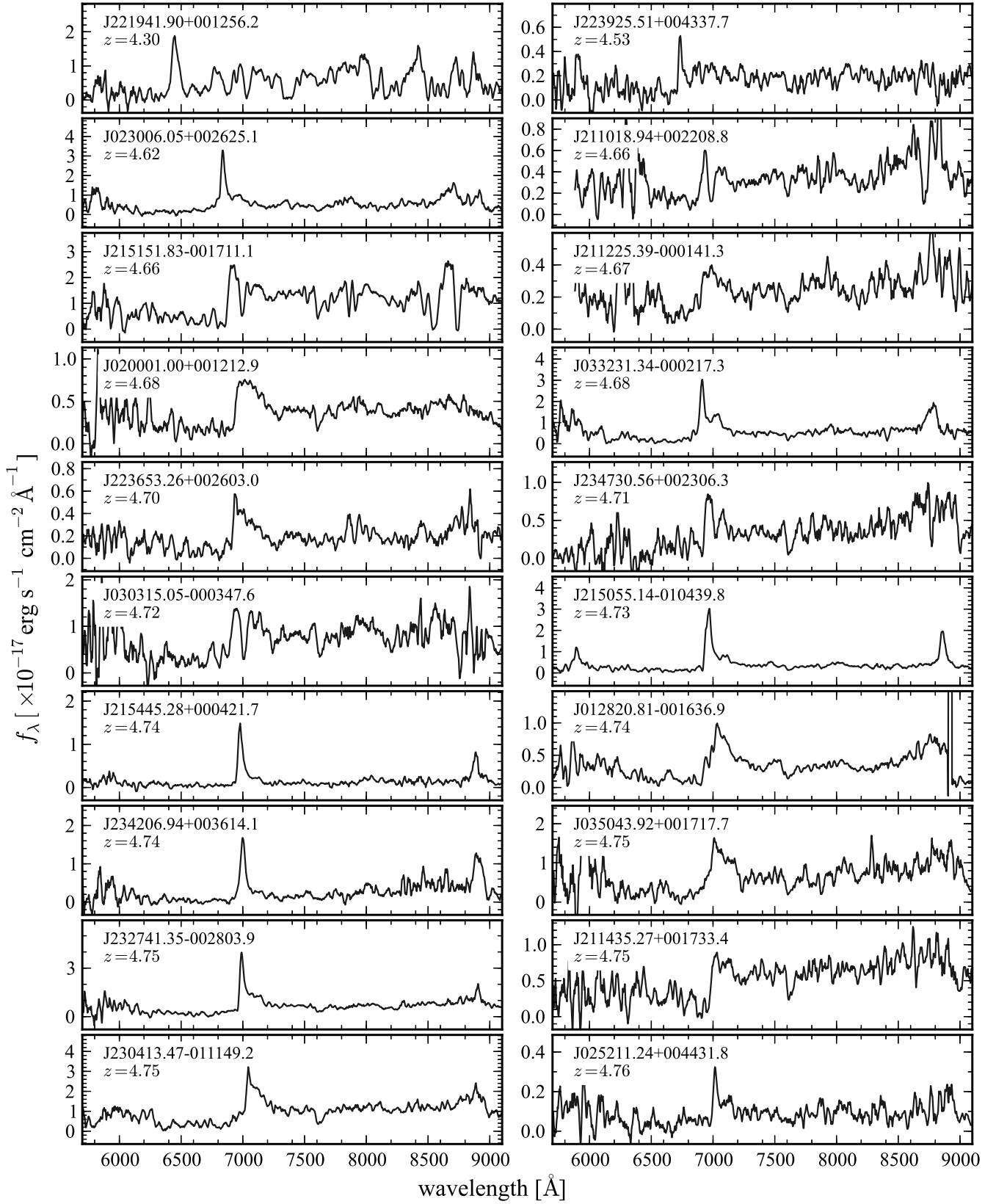


FIG. 21.— Spectra of Stripe 82 quasars observed with MMT Red Channel, smoothed with a 7 pixel boxcar. The MMT spectra are at low resolution ($R \sim 400$ – 600) and from short, 10–15m. observations, thus they have relatively lower S/N . We present the spectra with the nominal flux calibrations obtained from standard star observations; however, the absolute flux calibrations have considerable uncertainties.

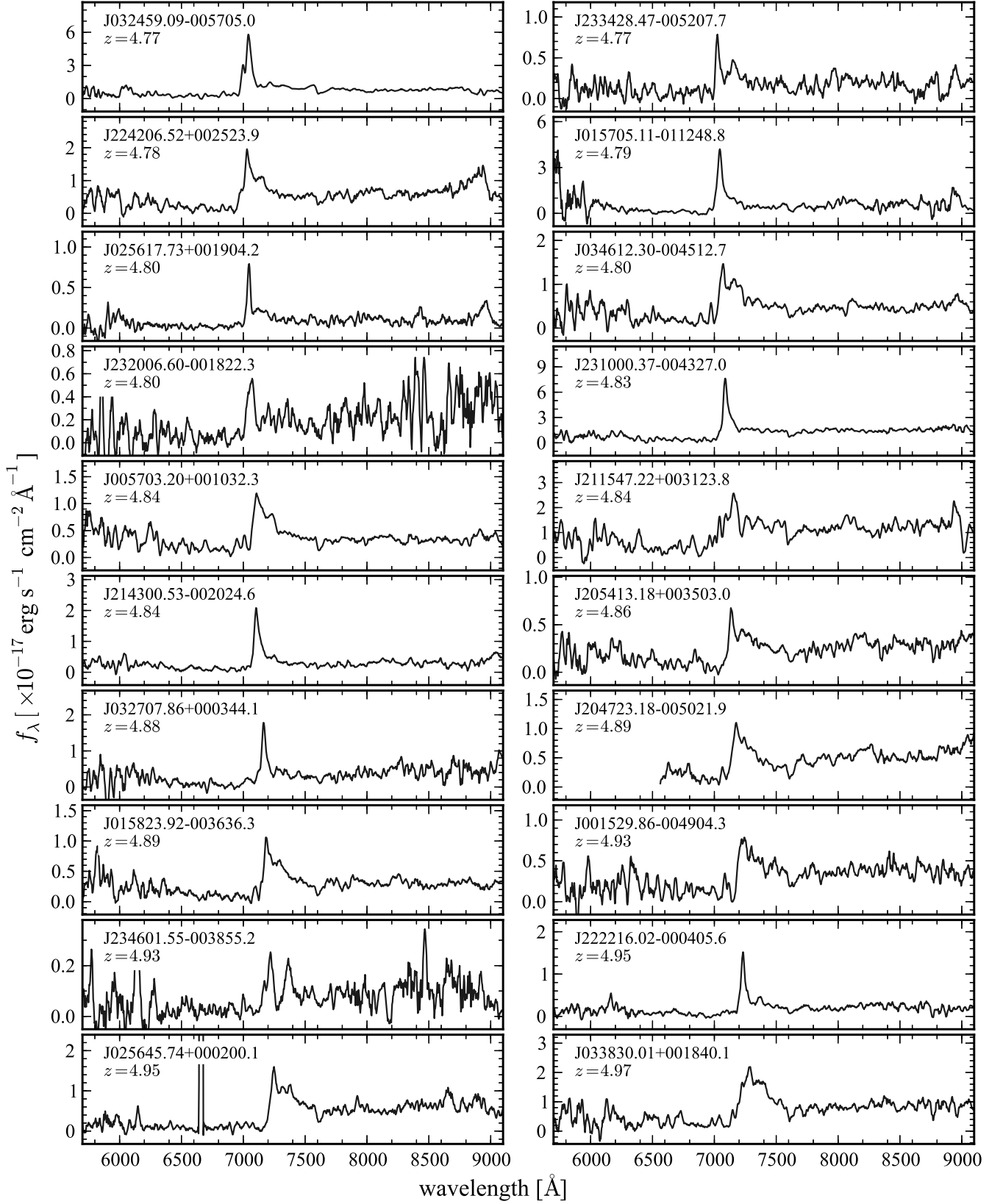


FIG. 22.— Spectra of Stripe 82 quasars observed with MMT Red Channel, continued.

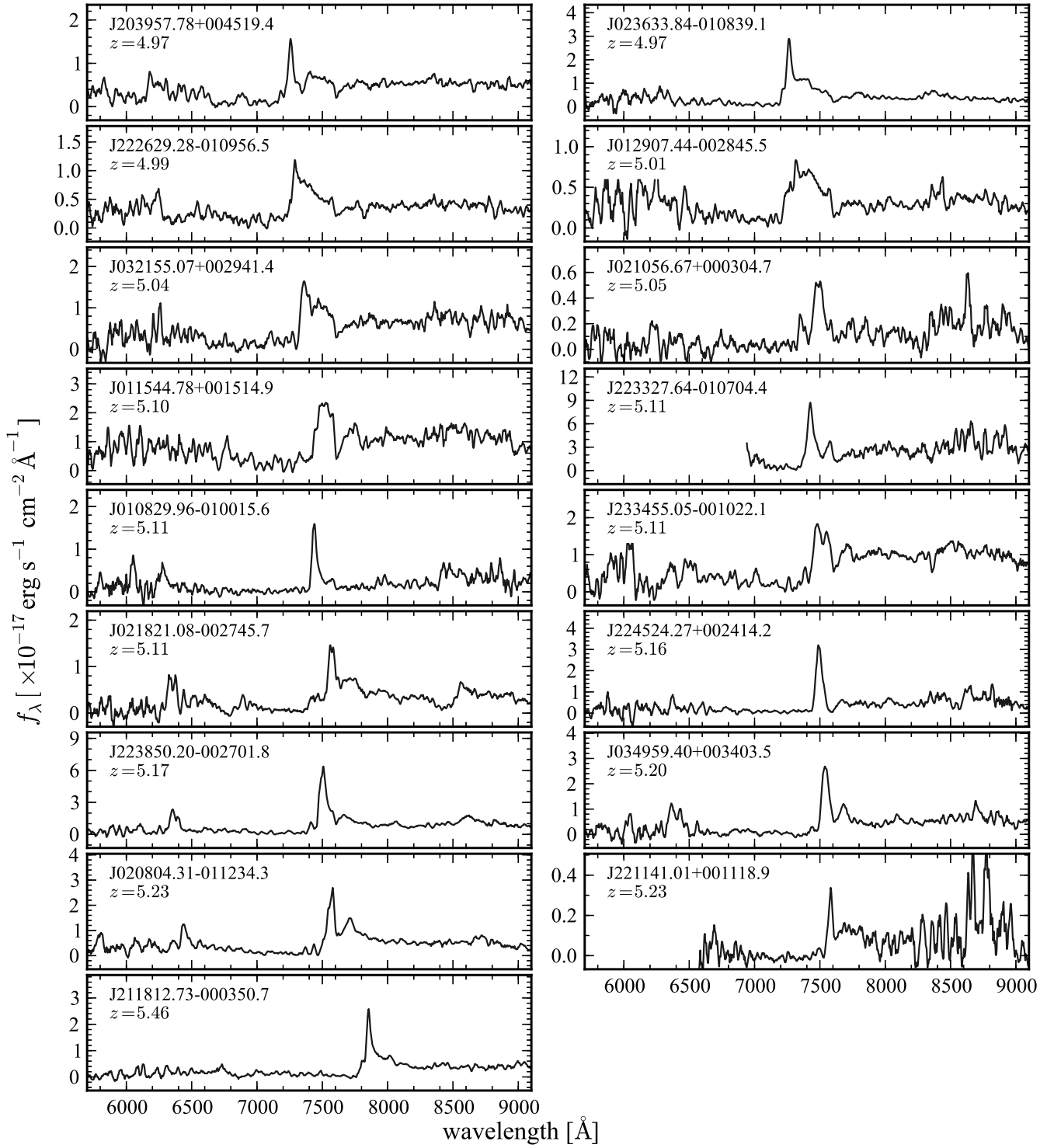


FIG. 23.— Spectra of Stripe 82 quasars observed with MMT Red Channel, continued.

TABLE 4
STRIPE 82 HIGH REDSHIFT QUASAR CATALOG

RA (J2000)	Dec (J2000)	g_{AB}	r_{AB}	i_{AB}	z_{AB}	J_{AB}	M_{1450}	z	p^a	Notes ^b
20:39:57.78	+00:45:19.4		23.37 ± 0.08	21.80 ± 0.03	21.63 ± 0.08	...	-24.42	4.97	0.46	20120528
20:47:23.18	-00:50:21.9		22.67 ± 0.04	21.34 ± 0.02	21.08 ± 0.05	...	-24.79	4.89	-1	20110624
20:54:13.18	+00:35:03.0		22.83 ± 0.05	21.59 ± 0.02	21.46 ± 0.07	...	-24.50	4.86	0.74	20120528
21:10:18.94	+00:22:08.8	24.99 ± 0.26	22.79 ± 0.05	21.32 ± 0.02	21.14 ± 0.06	...	-24.63	4.66	-1	20110623
21:11:58.01	+00:53:02.6		22.76 ± 0.05	21.00 ± 0.02	20.80 ± 0.04	21.16 ± 0.47	-25.29	4.98	-1	20110611
21:12:25.39	-00:01:41.3	24.93 ± 0.23	22.42 ± 0.03	20.98 ± 0.01	20.81 ± 0.04	...	-24.99	4.67	-1	20110623
21:14:35.27	+00:17:33.4	25.81 ± 0.53	22.64 ± 0.04	21.11 ± 0.01	20.93 ± 0.05	20.32 ± 0.06^c	-24.89	4.75	0.84	20111002
21:15:47.22	+00:31:23.8	24.97 ± 0.27	22.40 ± 0.03	20.83 ± 0.01	20.68 ± 0.04	...	-25.27	4.84	0.77	20120528
21:18:12.73	-00:03:50.7		23.72 ± 0.10	21.60 ± 0.02	21.18 ± 0.05	...	-25.64	5.46	-1	20120528
21:30:08.93	+00:26:09.8	26.41 ± 0.79	22.41 ± 0.03	20.21 ± 0.01	20.48 ± 0.03	...	-26.08	4.95	0.62	DR7
21:43:00.53	-00:20:24.6	26.18 ± 0.68	23.58 ± 0.09	21.94 ± 0.03	21.93 ± 0.11		-24.11	4.84	0.28	20120527
21:50:55.14	-01:04:39.8		23.15 ± 0.07	21.52 ± 0.03	21.55 ± 0.08		-24.45	4.73	0.79	20120527
21:51:51.83	-00:17:11.1	24.84 ± 0.27	22.44 ± 0.04	20.75 ± 0.01	20.55 ± 0.03	20.13 ± 0.05^c	-25.23	4.66	-1	20111002
21:54:45.28	+00:04:21.7		23.57 ± 0.09	21.91 ± 0.03	21.71 ± 0.11		-24.05	4.74	0.41	20120528
22:00:08.66	+00:17:44.9	24.11 ± 0.10	20.60 ± 0.01	19.05 ± 0.00	19.19 ± 0.01	19.27 ± 0.07	-27.11	4.82	0.88	DR7
22:11:41.01	+00:11:18.9		24.31 ± 0.17	21.88 ± 0.03	21.83 ± 0.12		-24.84	5.23	-1	20110624
22:12:51.50	-00:42:30.7	24.96 ± 0.25	21.64 ± 0.02	19.88 ± 0.00	20.03 ± 0.02	20.55 ± 0.25	-26.43	4.95	0.61	DR7
22:16:44.01	+00:13:48.1		21.94 ± 0.02	20.34 ± 0.01	20.18 ± 0.02	20.25 ± 0.17	-26.07	5.03	0.40	4200-55499-975
22:18:51.74	-01:02:59.0	25.97 ± 0.86	22.37 ± 0.03	20.79 ± 0.01	20.68 ± 0.03	20.83 ± 0.31	-25.23	4.74	0.84	4201-55443-370
22:19:41.90	+00:12:56.2	25.37 ± 0.33	22.93 ± 0.05	21.50 ± 0.02	21.29 ± 0.06	21.05 ± 0.10^c	-24.37	4.30	-1	20111002
22:20:18.48	-01:01:46.8		24.23 ± 0.16	21.65 ± 0.02	20.34 ± 0.02	20.42 ± 0.19	-25.83	5.62	-1	4201-55443-246
22:20:50.80	+00:19:59.1	23.83 ± 0.08	21.51 ± 0.01	20.08 ± 0.00	20.04 ± 0.02	19.74 ± 0.10	-25.95	4.72	0.90	DR7
22:22:16.02	-00:04:05.6	26.61 ± 0.98	23.81 ± 0.11	21.90 ± 0.03	21.83 ± 0.09	21.41 ± 0.40	-24.29	4.95	0.32	20120528
22:25:09.19	-00:14:06.8	22.73 ± 0.03	20.41 ± 0.00	18.98 ± 0.00	18.79 ± 0.01	18.86 ± 0.05	-27.28	4.89	0.72	DR7
22:26:29.28	-01:09:56.5		23.27 ± 0.07	21.69 ± 0.02	21.50 ± 0.07	20.76 ± 0.28	-24.57	4.99	0.55	20120527
22:33:27.64	-01:07:04.4		23.62 ± 0.09	21.52 ± 0.02	21.49 ± 0.07	...	-24.97	5.11	-1	20110624
22:36:53.26	+00:26:03.0	26.16 ± 0.66	23.63 ± 0.09	22.02 ± 0.03	22.10 ± 0.11	22.10 ± 0.76	-23.92	4.70	-1	20120528
22:38:50.20	-00:27:01.8	26.06 ± 0.60	23.11 ± 0.06	21.49 ± 0.02	21.36 ± 0.06	21.62 ± 0.17^c	-25.13	5.17	-1	20111002
22:38:59.79	+00:56:23.6	24.74 ± 0.61	22.88 ± 0.05	20.91 ± 0.01	20.96 ± 0.04	21.43 ± 0.51	-25.23	4.88	-1	4204-55470-710
22:39:07.56	+00:30:22.6		22.97 ± 0.05	21.24 ± 0.02	21.19 ± 0.05	21.04 ± 0.34	-25.23	5.09	0.33	20110613
22:39:25.51	+00:43:37.7	26.10 ± 0.65	23.23 ± 0.06	21.88 ± 0.03	21.81 ± 0.08		-24.11	4.53	-1	20120528
22:42:06.52	+00:25:23.9	25.41 ± 0.33	23.39 ± 0.07	21.85 ± 0.03	21.77 ± 0.10	21.73 ± 0.82	-24.14	4.78	0.52	20111002
22:45:24.27	+00:24:14.2	26.46 ± 0.92	23.75 ± 0.11	21.72 ± 0.02	21.86 ± 0.11	21.30 ± 0.12^c	-24.88	5.16	-1	20111002
22:04:13.47	-01:11:49.2	25.29 ± 0.37	22.78 ± 0.04	21.24 ± 0.02	21.14 ± 0.05	...	-24.75	4.75	0.84	20111002
23:09:16.76	+00:10:02.6	26.31 ± 0.68	22.62 ± 0.03	20.91 ± 0.01	20.99 ± 0.05	21.16 ± 0.27	-25.08	4.73	0.83	4208-55476-896
23:10:00.37	-00:43:27.0	25.48 ± 0.33	22.62 ± 0.03	20.88 ± 0.01	20.87 ± 0.04	...	-25.21	4.83	0.77	20111002
23:12:16.44	+01:00:51.5	25.60 ± 0.44	22.71 ± 0.04	20.87 ± 0.01	20.75 ± 0.03		-25.61	5.08	-1	4209-55478-714
23:20:06.60	-01:08:22.3	26.08 ± 0.54	23.48 ± 0.07	21.58 ± 0.02	21.73 ± 0.08	21.25 ± 0.39	-24.44	4.80	0.77	20111002
23:27:41.35	-00:28:03.9		23.64 ± 0.08	21.80 ± 0.02	21.84 ± 0.08		-24.17	4.75	0.59	20111002
23:32:23.57	+01:02:53.5		22.83 ± 0.04	21.12 ± 0.01	20.99 ± 0.04	20.66 ± 0.23	-24.95	4.83	-1	4212-55447-680
23:34:28.47	-00:52:07.7		23.80 ± 0.10	21.99 ± 0.03	22.18 ± 0.11		-23.99	4.77	0.25	20120527
23:34:55.05	-00:10:22.1		23.56 ± 0.07	21.82 ± 0.02	21.33 ± 0.05	20.85 ± 0.38	-24.65	5.11	-1	20111002
23:42:06.94	+00:36:14.1		23.30 ± 0.06	21.72 ± 0.02	21.74 ± 0.08	21.39 ± 0.13^c	-24.25	4.74	0.69	20111002
23:46:01.55	-00:38:55.2		23.64 ± 0.09	21.69 ± 0.02	21.56 ± 0.07		-24.49	4.93	0.62	20111001
23:47:30.56	+00:23:06.3	25.88 ± 0.41	22.72 ± 0.04	21.09 ± 0.01	20.75 ± 0.04	...	-24.89	4.71	0.81	20111002
00:05:52.33	-00:06:55.6		25.42 ± 0.42	23.05 ± 0.07	20.47 ± 0.02	...	-24.42	5.86	-1	4216-55477-019
00:07:49.16	+00:41:19.5	25.94 ± 0.54	21.46 ± 0.01	20.03 ± 0.00	19.93 ± 0.01	20.34 ± 0.12	-26.10	4.83	0.87	DR7
00:15:29.86	-00:49:04.3	25.57 ± 0.36	22.57 ± 0.03	21.01 ± 0.01	20.69 ± 0.03	20.56 ± 0.19	-25.20	4.93	0.68	20111001
00:23:30.67	-00:18:36.4		23.10 ± 0.05	21.31 ± 0.01	20.82 ± 0.03	21.50 ± 0.52	-25.10	5.06	0.44	4220-55447-474
00:35:25.29	+00:40:02.8	23.73 ± 0.07	21.38 ± 0.01	19.66 ± 0.00	19.71 ± 0.01	19.83 ± 0.09	-26.42	4.76	0.94	DR7
00:36:05.64	+01:03:45.1	25.17 ± 0.32	22.18 ± 0.02	20.83 ± 0.01	20.77 ± 0.03	20.78 ± 0.19	-25.17	4.72	-1	4221-55443-864
00:54:21.42	-01:09:21.6		21.28 ± 0.01	19.92 ± 0.00	19.54 ± 0.01	19.51 ± 0.09	-26.63	5.09	-1	DR7
00:57:03.20	+00:10:32.3		22.98 ± 0.05	21.45 ± 0.02	21.31 ± 0.07	21.12 ± 0.28	-24.61	4.84	0.78	20111001
01:08:29.96	-01:00:15.6		23.67 ± 0.10	21.85 ± 0.03	21.69 ± 0.07	21.35 ± 0.52	-24.63	5.11	-1	20111002
01:10:10.22	+00:24:19.5	25.07 ± 0.21	22.14 ± 0.02	20.73 ± 0.01	20.66 ± 0.03	21.37 ± 0.47	-25.26	4.71	0.80	4227-55481-528
01:15:44.78	+00:15:14.9	26.10 ± 0.58	22.97 ± 0.04	21.47 ± 0.02	21.09 ± 0.05	20.59 ± 0.06^c	-25.00	5.10	-1	20111003
01:21:35.57	+00:12:05.7	24.51 ± 0.12	22.37 ± 0.03	20.98 ± 0.01	21.02 ± 0.05	21.24 ± 0.45	-25.01	4.72	0.83	4228-55484-774
01:28:20.81	-00:16:36.9	25.39 ± 0.27	22.65 ± 0.03	21.20 ± 0.01	21.26 ± 0.05	21.12 ± 0.48	-24.79	4.74	0.84	20111001
01:29:07.44	-00:28:45.5		23.02 ± 0.04	21.54 ± 0.02	21.34 ± 0.05	21.31 ± 0.45	-24.77	5.01	0.58	20111001
01:57:05.11	-01:12:48.8	25.35 ± 0.33	23.73 ± 0.08	21.92 ± 0.03	21.98 ± 0.09	21.19 ± 0.47	-24.08	4.79	-1	20111003
01:58:23.92	-00:36:36.3		23.30 ± 0.05	21.62 ± 0.02	21.39 ± 0.05		-24.50	4.89	0.70	20111001
02:00:01.00	+00:12:12.9		23.15 ± 0.04	21.64 ± 0.02	21.40 ± 0.06	21.21 ± 0.11^c	-24.31	4.68	-1	20111001
02:08:04.31	-01:12:34.3		23.12 ± 0.05	21.46 ± 0.02	21.21 ± 0.04		-25.28	5.23	-1	20111001
02:10:43.16	-00:18:18.4	22.69 ± 0.02	20.43 ± 0.00	19.18 ± 0.00	19.09 ± 0.01	19.33 ± 0.06	-26.90	4.73	0.93	DR7
02:10:56.67	+00:03:04.7		23.97 ± 0.10	21.60 ± 0.02	21.41 ± 0.07	21.17 ± 0.10^c	-24.77	5.05	0.47	20111003
02:11:02.72	-00:09:10.1	24.56 ± 0.13	21.64 ± 0.01	20.05 ± 0.00	20.03 ± 0.01	20.20 ± 0.12	-26.19	4.92	0.71	4236-55479-475
02:18:21.08	-00:27:45.7		23.72 ± 0.09	21.65 ± 0.02	21.31 ± 0.04		-24.84	5.11	-1	20111001
02:30:06.05	+00:26:25.1	25.39 ± 0.25	22.94 ± 0.04	21.69 ± 0.02	21.46 ± 0.05	21.65 ± 0.59	-24.26	4.62	-1	20111002
02:36:33.84	-01:08:39.1	25.70 ± 0.46	23.34 ± 0.06	21.29 ± 0.01	21.43 ± 0.05	21.89 ± 0.82	-24.97	4.97	0.64	20111001
02:50:19.77	+00:46:50.4	22.99 ± 0.03	21.10 ± 0.01	19.68 ± 0.00	19.63 ± 0.01	19.90 ± 0.11	-26.43	4.80	0.91	4241-55450-836
02:52:11.24	+00:44:31.8	24.95 ± 0.21	22.55 ± 0.03	21.06 ± 0.01	21.12 ± 0.04	21.74 ± 0.72	-24.95	4.76	0.83	20111001
02:56:17.73	+00:19:04.2		23.56 ± 0.09	21.73 ± 0.02	21.83 ± 0.10	21.99 ± 0.13^c	-24			

TABLE 4 — *Continued*

RA (J2000)	Dec (J2000)	g_{AB}	r_{AB}	i_{AB}	z_{AB}	J_{AB}	M_{1450}	z	p^a	Notes ^b
03:21:55.07	+00:29:41.4		22.83 ± 0.04	21.44 ± 0.02	21.25 ± 0.05		-24.92	5.04	0.52	20111002
03:24:59.09	-00:57:05.0	25.86 ± 0.71	22.53 ± 0.03	20.30 ± 0.01	20.37 ± 0.02	20.01 ± 0.10	-25.76	4.77	0.87	20111001
03:27:07.86	+00:03:44.1		23.11 ± 0.06	21.45 ± 0.02	21.45 ± 0.07	21.63 ± 0.35	-24.66	4.88	0.75	20111002
03:32:31.34	-00:02:17.3	26.20 ± 0.71	22.94 ± 0.04	21.60 ± 0.02	21.60 ± 0.07	21.90 ± 0.43	-24.35	4.68	-1	20111002
03:38:29.31	+00:21:56.3	25.76 ± 0.46	21.39 ± 0.01	19.84 ± 0.00	19.60 ± 0.01	19.83 ± 0.08	-26.61	5.03	0.35	DR7
03:38:30.01	+00:18:40.1	26.60 ± 1.00	22.75 ± 0.04	21.16 ± 0.01	21.03 ± 0.05	21.48 ± 0.37	-25.09	4.97	0.64	20111002
03:46:12.30	-00:45:12.7		22.07 ± 0.03	20.49 ± 0.01	20.46 ± 0.03	20.80 ± 0.39	-25.59	4.80	0.83	20111001
03:49:59.40	+00:34:03.5		23.54 ± 0.11	21.38 ± 0.02	21.27 ± 0.06	21.28 ± 0.30	-25.31	5.20	-1	20111002
03:50:43.92	+00:17:17.7	25.27 ± 0.47	22.56 ± 0.05	21.28 ± 0.02	21.43 ± 0.10		-24.72	4.75	0.84	20111003

NOTE. — Magnitudes are on the AB system (Oke & Gunn 1983) and have been corrected for extinction. Blank entries indicate objects for which SExtractor did not report a magnitude in that band (due to negative fluxes); objects that are not formally detected but have measurements from SExtractor are included with their uncertainties. Ellipses indicate lack of coverage.

^a The selection probability $p(M, z)$ of spectroscopically confirming this object, including all sources of incompleteness (see §6.1.2). A value of -1 indicates an object not included in the uniform sample.

^b Spectroscopic identifications from MMT/Magellan show the UT date of the observation; those from BOSS give the plate-MJD-fiber of the observation.

^c J magnitude from SWIRC.

TABLE 5
STRIPE 82 HIGH REDSHIFT QUASAR TARGETS

RA (J2000)	Dec (J2000)	g_{AB}	r_{AB}	i_{AB}	z_{AB}	J_{AB}	Notes
20:37:53.64	+00:05:49.4		22.81 ± 0.05	20.84 ± 0.01	20.33 ± 0.03	...	
20:49:47.51	+00:08:24.1	25.82 ± 0.59	23.38 ± 0.09	21.91 ± 0.03	21.64 ± 0.11	...	star
20:59:54.11	-00:54:27.7	25.90 ± 0.76	23.11 ± 0.06	21.54 ± 0.02	21.24 ± 0.05	21.22 ± 0.15^a	
21:00:41.31	-00:52:03.4	25.58 ± 0.58	23.59 ± 0.10	21.79 ± 0.03	21.37 ± 0.06	20.94 ± 0.10^a	
21:05:17.96	-00:49:20.2		23.23 ± 0.07	21.49 ± 0.02	21.18 ± 0.06	20.86 ± 0.31	
21:47:30.25	+00:12:37.5	25.32 ± 0.38	23.65 ± 0.11	21.92 ± 0.03	21.50 ± 0.09	20.82 ± 0.38	
21:52:56.25	-01:06:13.8	25.01 ± 0.46	23.00 ± 0.07	21.56 ± 0.03	21.32 ± 0.07	20.66 ± 0.08^a	
00:03:32.25	+00:37:49.9	26.30 ± 0.72	23.18 ± 0.05	21.61 ± 0.02	21.37 ± 0.05	21.30 ± 0.32	
00:05:31.71	-00:34:43.4		23.85 ± 0.10	21.91 ± 0.03	21.75 ± 0.07	21.77 ± 0.64	
00:18:22.10	+00:25:23.1	26.20 ± 0.64	23.61 ± 0.08	21.79 ± 0.02	21.68 ± 0.08	...	
00:23:53.63	-00:43:56.9	26.00 ± 0.52	23.64 ± 0.08	21.51 ± 0.02	21.00 ± 0.04	20.75 ± 0.07^a	
00:30:30.36	-00:04:17.7	25.78 ± 0.42	23.41 ± 0.06	21.78 ± 0.02	21.67 ± 0.06	21.69 ± 0.76	
00:41:37.17	-00:30:39.4		22.94 ± 0.04	20.92 ± 0.01	20.45 ± 0.02	20.00 ± 0.15	
01:26:55.05	-00:00:12.7		24.37 ± 0.16	21.87 ± 0.02	21.78 ± 0.10	21.09 ± 0.40	star
01:40:14.61	-00:12:59.9	25.42 ± 0.30	23.30 ± 0.05	22.00 ± 0.02	21.81 ± 0.07	21.47 ± 0.60	
02:38:09.21	-01:09:27.5	28.23 ± 4.72	23.44 ± 0.06	21.94 ± 0.03	21.83 ± 0.08	...	
02:52:29.91	-00:48:13.1		23.74 ± 0.09	21.97 ± 0.03	21.77 ± 0.08	21.14 ± 0.41	
03:09:37.66	+00:46:16.8	26.77 ± 1.16	23.32 ± 0.06	21.91 ± 0.03	21.74 ± 0.07	21.38 ± 0.37	
03:40:50.33	+00:48:12.2	25.99 ± 0.61	23.23 ± 0.07	21.88 ± 0.03	21.73 ± 0.07	21.06 ± 0.23	
03:54:23.45	+00:32:31.6	24.00 ± 0.44	22.92 ± 0.15	21.28 ± 0.04	21.05 ± 0.08	20.33 ± 0.18	
03:56:55.52	-00:34:47.9	24.82 ± 0.65	22.48 ± 0.08	21.21 ± 0.03	21.09 ± 0.07	22.01 ± 1.16	

NOTE. — Targets selected by our color criteria that either lack spectroscopic observations or are confirmed non-quasars. Magnitudes are given in the same format as Table 4.

^a J magnitude from SWIRC.